Oxygen Release and Its Effect on the Cycling Stability of LiNi$_x$Mn$_y$Co$_z$O$_2$ (NMC) Cathode Materials for Li-Ion Batteries

Roland Jung,[a,b,*,z] Michael Metzger,[a,*] Filippo Maglia,[b] Christoph Stinner,[b] and Hubert A. Gasteiger[a,**]

[a]Chair of Technical Electrochemistry, Department of Chemistry and Catalysis Research Center, Technische Universität München, Garching, Germany
[b]BMW AG, Munich, Germany

Layered LiNi$_x$Mn$_y$Co$_z$O$_2$ (NMC) is a widely used class of cathode materials with LiNi$_{1/3}$Mn$_{1/3}$Co$_{1/3}$O$_2$ (NMC111) being the most common representative. However, Ni-rich NMCs are more and more in the focus of current research due to their higher specific capacity and energy. In this work we will compare LiNi$_{1/3}$Mn$_{1/3}$Co$_{1/3}$O$_2$ (NMC111), LiNi$_{0.6}$Mn$_{0.2}$Co$_{0.2}$O$_2$ (NMC622), and LiNi$_{0.8}$Mn$_{0.1}$Co$_{0.1}$O$_2$ (NMC811) with respect to their cycling stability in NMC-graphite full-cells at different end-of-charge potentials. It will be shown that stable cycling is possible up to 4.4 V for NMC111 and NMC622 and only up to 4.0 V for NMC811. At higher potentials, significant capacity fading was observed, which was traced back to an increase in the polarization of the NMC electrode, contrary to the nearly constant polarization of the graphite electrode. Furthermore, we show that the increase in the polarization occurs when the NMC materials are cycled up to a high-voltage feature in the dq/dV plot, which occurs at ∼4.7 V vs. Li/Li$^+$ for NMC111 and NMC622 and at ∼4.3 V vs. Li/Li$^+$ for NMC811. For the latter material, this feature corresponds to the H2 → H3 phase transition. Contrary to the common understanding that the electrochemical oxidation of carbonate electrolytes causes the CO$_2$ and CO evolution at potentials above 4.7 V vs. Li/Li$^+$, we believe that the observed CO$_2$ and CO are mainly due to the chemical reaction of reactive lattice oxygen with the electrolyte. This hypothesis is based on gas analysis using On-line Electrochemical Mass Spectrometry (OEMS), by which we prove that all three materials release oxygen from the particle surface and that the oxygen evolution coincides with the onset of CO$_2$ and CO evolution. Interestingly, the onsets of oxygen evolution for the different NMCs correlate well with the high-voltage redox feature at ∼4.7 V vs. Li/Li$^+$ for NMC111 and NMC622 as well as at ∼4.3 V vs. Li/Li$^+$ for NMC811. To support this hypothesis, we show that no CO$_2$ or CO is evolved for the LiNi$_{0.43}$Mn$_{1.57}$O$_4$ (LNMO) spinel up to 5 V vs. Li/Li$^+$, consistent with the absence of oxygen release. Lastly, we demonstrate by the use of ^{13}C labeled conductive carbon that it is the electrolyte rather than the conductive carbon which is oxidized by the released lattice oxygen. Taking these findings into consideration, a mechanism is proposed for the reaction of released lattice oxygen with ethylene carbonate yielding CO$_2$, CO, and H$_2$O.

Li-Ion batteries have recently been used as power supply for electric vehicles (EVs). In order to penetrate the mass market, a significant reduction in costs and further performance improvements have to be achieved to realize a longer driving range of EVs.[1] The latter highly depends on the choice of the cathode active material, for which several potential materials exist,[2] of which layered lithium nickel manganese cobalt oxide (LiNi$_x$Mn$_y$Co$_z$O$_2$, NMC) is one of the most promising class of cathode materials.[3] This is due to the high specific capacity and good stability of the layered structure which changes its volume by less than 2% during Li insertion/extraction.[4–6] Due to the sloped voltage profile of NMC, a higher capacity and energy density can be achieved when the upper cutoff voltage is increased.[7–9] Even though the theoretical capacity of NMC is as high as ∼275 mAh/g$_{NMC}$, not all of the lithium can be extracted due to structural instabilities occurring when an exceedingly large fraction of lithium is removed.[9,10] Additionally, the sloped voltage profile requires very high voltages to achieve complete removal of lithium, which in turn can lead to electrolyte oxidation, surface film formation, and transition metal dissolution, ultimately diminishing the cycling stability.[11–17] For these reasons, the operating potential of NMC based cathode materials is nowadays limited to ∼4.3 V, restricting their capacities to much below their theoretical values.[5] In order to improve the accessible capacity at reasonable upper cutoff voltages, Ni-rich NMCs (Ni-content >> Mn- and Co-content) recently became the focus of interest, as more lithium can be extracted from their structure within the same voltage window. Therefore, they provide larger specific capacities and energy densities, which are crucial for a longer driving range of electric vehicles.[2,18,19]

So far, however, Ni-rich NMCs suffer from a shorter lifetime due to a faster capacity fading compared to LiNi$_{1/3}$Mn$_{1/3}$Co$_{1/3}$O$_2$ (NMC111), the most common NMC material with a nickel:manganese:cobalt ratio of 1:1:1.[18–20] For example, Noh et al. reported initial capacities at a 0.1 C-rate and an end-of-charge potential of 4.3 V vs. Li/Li$^+$ of 203 mAh/g and 163 mAh/g for LiNi$_{0.8}$Mn$_{0.1}$Co$_{0.1}$O$_2$ (NMC811) and NMC111, respectively.[18] Unfortunately, the capacity retention for NMC811 in NMC-Li cells after 100 cycles at a 0.5 C-rate was only 70% compared to 92% for NMC111.[18] Furthermore, it was shown that layered oxides with rising Ni-contents are thermally less stable.[18,21] At temperatures ≥170°C, the bulk materials undergo a two-phase transition from their layered structure to a spinel structure and eventually to a rock-salt structure, both of which are accompanied by release of lattice oxygen.[18,21–27] For materials aged under battery operating conditions (<60°C), the formation of disordered spinel and rock-salt type phases was reported to happen on the particle surface with the bulk structure remaining intact, i.e., remaining in the rhombohedral structure as reported for NMC,[9] LiNi$_{0.8}$Co$_{0.2}$O$_2$,[28,29] LiNiO$_2$,[30] and NCA (LiNi$_{0.80}$Co$_{0.15}$Al$_{0.05}$O$_2$).[31] Even though it was not explicitly shown in these latter reports, the observed phase transitions suggest a release of oxygen from the particle surface, which was also pointed out in the reports by Abraham et al., Muto et al., and Hwang et al.[28–31] So far, a release of oxygen from the oxide lattice under battery operating conditions was shown only for overlithiated NMC materials (Li$_{1+x}$(Ni,Mn,Co)$_{1-x}$O$_2$), in which lithium additionally occupies the transition metal layers.[32–36] The exception is a recent publication by Guéguen et al., who showed oxygen evolution during battery cycling for NMC111.[37]

In this study, we will compare two Ni-rich NMCs, namely LiNi$_{0.6}$Mn$_{0.2}$Co$_{0.2}$O$_2$ (NMC622) and LiNi$_{0.8}$Mn$_{0.1}$Co$_{0.1}$O$_2$ (NMC811) to LiNi$_{1/3}$Mn$_{1/3}$Co$_{1/3}$O$_2$ (NMC111) with respect to their cycling

*Electrochemical Society Student Member.
**Electrochemical Society Fellow.
^{z}E-mail: roland.jung@tum.de

stability in full-cells with graphite anodes. Through an evaluation of the anode and cathode polarization in a three-electrode set-up, we conclude that the capacity fading at high voltages is due to the NMC electrode rather than the graphite electrode. By means of On-line Electrochemical Mass Spectrometry (OEMS) we prove that at high degrees of delithiation all three NMC materials release oxygen already at room temperature. The onset of the oxygen evolution corresponds well with the onset of the formation of CO_2 and CO, which is typically assigned to electrochemical electrolyte oxidation, raising the question whether the evolution of O_2 actually causes the observed CO_2 and CO evolution. This question as well as the consequences of the oxygen release on the polarization and the cycling stability will be discussed with the experimental findings presented in this work.

Experimental

Electrode Preparation.—Layered NMC and spinel LNMO electrodes were prepared by dispersing the active material particles ($LiNi_{1/3}Mn_{1/3}Co_{1/3}O_2$ (NMC111), $LiNi_{0.6}Mn_{0.2}Co_{0.2}O_2$ (NMC622), $LiNi_{0.8}Mn_{0.1}Co_{0.1}O_2$ (NMC811) or $LiNi_{0.43}Mn_{1.57}O_4$ (LNMO), all from Umicore, Belgium) ($91.5 \%_{wt}$), conductive carbon (Super C65, Timcal, Switzerland) ($4.4 \%_{wt}$) and polyvinylidene fluoride binder (PVDF, Kynar HSV 900, Arkema, France) ($4.1 \%_{wt}$) in N-methylpyrrolidone (NMP, anhydrous, 99.5%, Sigma-Aldrich). The slurry was mixed in a planetary mixer (Thinky, USA) at 2000 rpm for 2×5 minutes. In between the two runs the slurry was ultrasonicated for 10 minutes in an ultrasonic bath. The resulting ink was spread onto aluminum foil (thickness 18 μm, MTI Corporation, USA) using a gap bar coater (RK PrintCoat Instruments, UK). For OEMS measurements, the ink was coated onto a H2013 polyolefin separator (Celgard, USA) or a stainless steel mesh (316 grade, 26 μm aperture, 25 μm wire diameter, The Mesh Company, UK) to allow for a short diffusion time of the evolved gases to the head-space of the OEMS cell and to the capillary leading to the mass spectrometer.[38,39] NMC622 electrodes containing ¹³C-labeled carbon (99 $\%_{atom}$ ¹³C, Sigma-Aldrich, Germany) were prepared with the same composition as the ones containing Super C65, however, due to strong agglomeration of the carbon, the ink was prepared in a ball mill (Pulverisette 7, Fritsch, Germany) using zirconia balls with a diameter of 10 mm at 180 rpm for 60 minutes. After drying at 50°C, electrodes were punched and dried overnight at 120°C (if coated on aluminum or stainless steel mesh) and at 95°C (if coated on H2013 separator) under dynamic vacuum in a glass oven (drying oven 585, Büchi, Switzerland) and transferred to a glove box (O_2 and $H_2O < 0.1$ ppm, MBraun, Germany) without exposure to ambient air.

The graphite electrodes were composed of graphite (MAG-D20, Hitachi), Super C65 (Timcal, Switzerland), sodium carboxymethylcellulose (Na-CMC, Dow Wolff Cellulosics) and styrene-butadiene rubber (SBR, JSR Micro) at a weight ratio of 95.8:1:1:2.2. The slurry was prepared by dispersing graphite, Super C65 and Na-CMC in highly pure water (18 MΩ cm, Merck Millipore, Germany) using a planetary mixer (Thinky, USA; at 2000 rpm for 30 minutes). The slurry was ultrasonicated for 10 minutes in an ultrasonic bath. SBR was added to the slurry and mixed at 500 rpm for 2 minutes. The ink was coated onto copper foil (thickness 12 μm, MTI Corporation, USA) using a gap bar coater (RK PrintCoat Instruments, UK). The coating was dried at 50°C in air, punched out, dried overnight at 120°C under vacuum in a glass oven (Büchi oven, s. above) and transferred to a glove box without exposure to ambient air.

The specific surface areas of the NMC and LNMO were determined by BET, using an Autosorb iQ nitrogen gas sorption analyzer (Quantachrome Instruments, USA). The determined BET areas of these materials are $0.26 \ m^2/g$, $0.35 \ m^2/g$, $0.18 \ m^2/g$, and $0.23 \ m^2/g$ for NMC111, NMC622, NMC811, and LNMO, respectively.

Electrochemical characterization.—The electrochemical characterization of NMC was performed in Swagelok T-cells which were assembled in an argon filled glove box (O_2 and $H_2O < 0.1$ ppm, MBraun, Germany), with NMC as working electrode (10 mm diameter)

and graphite as counter electrode (11 mm diameter). The areal mass loading of the NMC electrodes was $15.5 \pm 1 \ mg/cm^2$ and the one of the graphite electrodes was adapted according to the mass loading of the NMC electrodes and their specific capacities at the various cutoff voltages, aiming to achieve a constant balancing factor. The areal capacity of the anode (in mAh/cm^2) was 1.2-fold oversized compared to the cathode (referenced to the reversible capacities of NMC and graphite at a 1 C-rate; if referenced to 0.1 C, the anode is roughly 1.1-fold oversized). To monitor the potential of both the NMC cathode and the graphite anode, a lithium reference electrode (thickness 0.45 mm, battery grade foil, 99.9 %, Rockwood Lithium, USA) was used. Two glass fiber separators (glass microfiber filter, 691, VWR, Germany) punched to a diameter of 11 mm were used between working and counter electrode, and one at the reference electrode (diameter of 10 mm). 80 μL of LP57 electrolyte (1 M $LiPF_6$ in EC:EMC 3:7 wt/wt, < 20 ppm H_2O, BASF, Germany) were used between working and counter electrode and 40 μL were added to the reference electrode side. The cells were cycled in a climate chamber (Binder, Germany) at 25°C with a battery cycler (Series 4000, Maccor, USA). All cells were cycled 300 times at 1 C with a lower cutoff of 3 V and an upper cutoff of 4.2, 4.4, or 4.6 V for NMC111 and NMC622, and 4.0, 4.1, 4.2 V for NMC811. Prior to cycling, the formation of the cells was done with 2 cycles at 0.1 C in the voltage range between 3 V and 4.2 V. If the upper cutoff was >4.2 V, the first cycle after formation, i.e., the third cycle of the cell was also done at 0.1 C to the specified upper cutoff. For upper cutoff voltages <4.2 V, i.e., for the NMC811 cells also the upper cutoff during formation was adapted to this voltage. The C-rate was referenced to the approximate reversible capacity of the NMC at 1 C: i) 140, 160, and 180 mAh/g for NMC111 at upper cutoff voltages of 4.2, 4.4, and 4.6 V, respectively; ii) 160, 180, and 200 mAh/g for NMC622 at upper cutoff voltages of 4.2, 4.4, and 4.6 V, respectively; and, iii) 130, 150, and 170 mAh/g for NMC811 at cutoff voltages of 4.0, 4.1, and 4.2 V, respectively. The charge was done in constant current-constant voltage (CCCV) mode with a current limitation corresponding to C/20, while the discharge was done in constant current (CC) mode. Two cells were built for each combination of NMC material and cutoff voltage and the error bars in the figures represent the standard deviation from two cells for each combination.

For recording dq/dV plots, NMC-graphite full-cells were assembled as described above and were cycled in a climate chamber (Binder, Germany) at 25°C with a battery cycler (Series 4000, Maccor, USA). The formation of the cells was done at 0.1 C (two cycles) in the voltage range between 3 V and 4.2 V. In the third cycle, the cutoff voltage was increased to 4.8 V. The lower cutoff was kept constant at 3 V. The dq/dV plot of the third cycle will be shown in the Results section.

On-line electrochemical mass spectrometry (OEMS).—Two different types of OEMS experiments were designed and performed with either NMC or spinel LNMO (diameter 15 mm) as working electrode, and either metallic lithium or graphite as counter electrode. With metallic lithium as counter electrode (lithium metal foil, diameter 16 mm, thickness 0.45 mm, battery grade foil, 99.9 %, Rockwood Lithium, USA), two H2013 polyolefin separators (diameter 28 mm, Celgard, USA) and 120 μL of LP57 electrolyte (1 M $LiPF_6$ in EC:EMC 3:7 wt/wt, < 20 ppm H_2O, BASF, Germany) were employed. The cells were charged up to 5 V at a 0.05 C-rate (referenced to the theoretical capacities of NMC111, NMC622, NMC811, and LNMO of 277.8 mAh/g, 276.5 mAh/g, 275.5 mAh/g, and 147 mAh/g, respectively). The loadings of the cathodes were 15.8 mg/cm^2 (NMC111), 15.5 mg/cm^2 (NMC622), 15.0 mg/cm^2 (NMC811), and 17.5 mg/cm^2 (LNMO). All electrodes were coated on H2013 separator (Celgard, USA).

With graphite as the counter electrode (diameter 16 mm, see upper section for details on the type of graphite), two glass fiber separators (diameter 28 mm, glass microfiber filter, 691, VWR, Germany) and 400 μL of 1.5 M $LiPF_6$ in ethylene carbonate (EC, BASF, Germany) were employed. The mixture of EC with $LiPF_6$ is a liquid at room temperature due to the melting point depression caused by the addition

of LiPF$_6$. The cells were cycled 4 times at a 0.2 C-rate (referenced to the above given theoretical capacities of the NMC materials) in the voltage range 2.6–4.8 V for NMC111 and NMC622 and from 2.6–4.4 V for NMC811. The loadings of the cathode active material were 9.4 mg/cm^2 (NMC111), 11.4 mg/cm^2 (NMC622), and 9.3 mg/cm^2 (NMC811) and the electrodes were coated on stainless steel mesh (see above for details). The graphite counter electrode was capacitively 1.4-fold oversized (referenced to the theoretical capacities of NMC and graphite).

All cells were assembled in a glove box with argon atmosphere (O$_2$ and H$_2$O < 0.1 ppm, MBraun, Germany). The cells were placed in a climate chamber at 25°C (Binder, Germany) and connected to the potentiostat (Series G300 potentiostat, Gamry, USA) and the mass spectrometer system, which has been described in detail elsewhere.[39] The cells were held at OCV for 4 h before starting the above described protocols. The gas evolution during the OCV and the charging/cycling period was recorded by OEMS. All mass signals were normalized to the ion current of the ^{36}Ar isotope to correct for fluctuations of pressure and temperature. Conversion of the ion currents to concentrations was done for O$_2$, CO$_2$, H$_2$, C$_2$H$_4$, and CO using calibration gases (Ar with 2000 ppm each of H$_2$, O$_2$, C$_2$H$_4$, and CO$_2$ as well as Ar with 2000 ppm each of H$_2$, O$_2$, CO, and CO$_2$; Westfalen, Germany) and based on a cell volume of 9.5 cm^3. Unlike all other gases quantified in this work, CO does not have a unique m/z channel. Therefore the amount of CO was determined on channel m/z = 28, which was corrected for the fractions of C$_2$H$_4$ and CO$_2$ both of which give additional intensity to channel m/z = 28. The fraction of the signal on channel m/z = 28 stemming exclusively from CO was therefore calculated as the total signal on channel m/z = 28 subtracted by 1.51 times the signal on channel m/z = 26 and 0.14 times the signal on channel m/z = 44, with the factors 1.51 and 0.14 being the fractions of C$_2$H$_4$ and CO$_2$ on channel m/z = 28 compared to their unique signals on m/z = 26 (C$_2$H$_4$) and m/z = 44 (CO$_2$), respectively. These factors were determined by flowing pure C$_2$H$_4$ and CO$_2$ through the OEMS cell and recording the resulting signals originating from the pure gases.[40]

Results

Electrochemical cycling of NMC-graphite cells.—Figure 1a shows the cycling stability of NMC111-graphite full-cells with different upper cutoff voltages of 4.2, 4.4, and 4.6 V. The cells have a very stable cycling performance for upper cutoff voltages of 4.2 V and 4.4 V (black and gray lines), however, cycling to 4.6 V leads to a fast capacity fading (light gray line), which is in agreement with previous reports in the literature.[9,11,13] While the error bars are hardly visibly for cutoff voltages ≤4.4 V and at low cycle numbers at a cutoff of 4.6 V, the error bars at higher cycle numbers significantly increase, which is due to the delayed onset of the so-called rollover-failure for the two cells. This failure mechanism was described previously by Dubarry et al. and Burns et al. and was shown to be due to growing kinetic resistances or more generally an impedance buildup.[41,42] In our data the increasing polarization stems almost exclusively from the NMC cathodes, which will be discussed below. The coulombic efficiencies (right axis in Figure 1a) for cells cycled to 4.2 V and 4.4 V are in average >99.9%, indicating the absence of major side reactions. When the end-of-charge voltage is increased to 4.6 V, the coulombic efficiency decreases to ~99.6% (before the onset of the rollover-failure), reflecting an increasing loss of cyclable lithium. A further decrease of the coulombic efficiency is observed at the onset of the rollover-failure. On the other hand, any increase in the polarization during cell discharge can be monitored by plotting the charge-averaged mean discharge voltage, defined as:

$$\bar{V}_{discharge} = \int V_{discharge} \cdot dq_{discharge} / \int dq_{discharge} \qquad [1]$$

As the cells were cycled with a lithium reference electrode, $\bar{V}_{discharge}$ can be determined independently for the NMC111 cathode ($\equiv \bar{V}_{discharge}^{cathode}$) and the graphite anode ($\equiv \bar{V}_{discharge}^{anode}$) for each end-of-charge voltage as a function of the cycle number, which is depicted in Figure 1b by the solid and dashed lines, respectively. While the energy
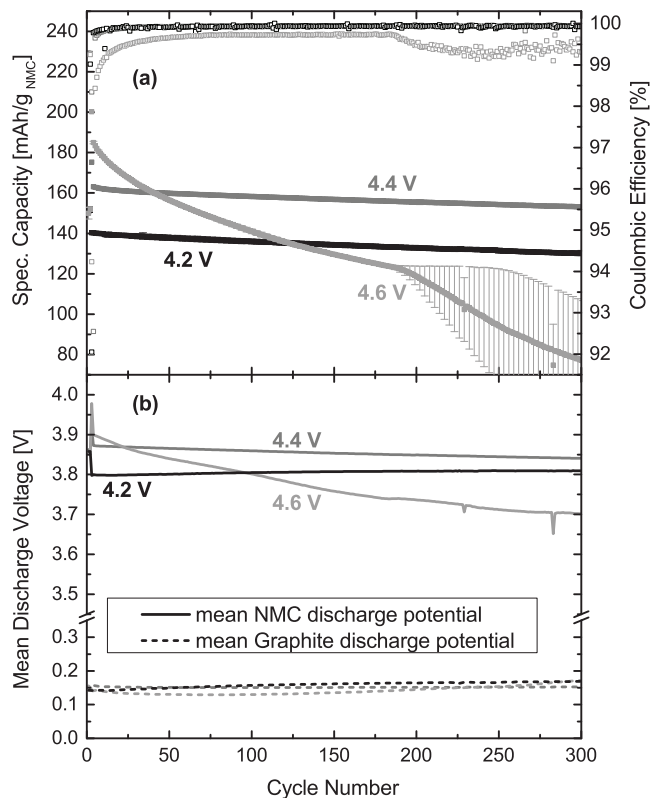

Figure 1. (a) Specific discharge capacity and coulombic efficiency of NMC111-graphite cells and (b) charge-averaged mean discharge voltage (s. Eq. 1) of the NMC111 cathode ($\equiv \bar{V}_{discharge}^{cathode}$; solid lines) and the graphite anode ($\equiv \bar{V}_{discharge}^{anode}$; dashed lines) vs. cycle number in LP57 electrolyte (1 M LiPF$_6$ in EC:EMC 3:7) operated with different upper cutoff voltages (4.2 V, 4.4 V, 4.6 V) and a constant lower cutoff voltage of 3.0 V. Formation was done at a rate of 0.1 C. Cycling was performed at 1 C and 25°C. For each condition, two independent cells were run and the data in the figure always represent the average of two cells (the error bars in (a) represent the standard deviation between the two cells).

fading of the cells is further detailed in the Discussion section, it may be noted here that the discharge energy for each cycle corresponds to the product of capacity and $\bar{V}_{discharge} = \bar{V}_{discharge}^{cathode} - \bar{V}_{discharge}^{anode}$. Under conditions where the loss of cyclable lithium is the only aging mechanism, i.e., in the absence of an impedance buildup, $\bar{V}_{discharge}^{cathode}$ for cathode active materials with a strongly sloping charge/voltage curve like NMC would be expected to gradually increase with the number of cycles. This can indeed be seen when cycling with an upper cutoff potential of 4.2 V (solid black line in Figure 1b). On the other hand, when impedance buildup becomes dominant, $\bar{V}_{discharge}^{cathode}$ decreases with the number of cycles, as can be seen when the upper cutoff potential reaches 4.6 V (solid light gray line in Figure 1b). Interestingly, the charge-averaged mean discharge voltages of the graphite anodes ($\bar{V}_{discharge}^{anode}$) remain fairly constant over the complete number of cycles, even at high end-of-charge voltages. This suggests that a crucial contributing factor for the fast capacity fading of the NMC111-graphite cells at an upper cutoff of 4.6 V is a strong impedance buildup on the NMC111 cathode rather than on the graphite anode. In fact, previous reports in the literature showed a drastic rise of the low frequency semicircle in the impedance spectra of NMC111-graphite[11] and NMC442-graphite cells,[43,44] which was attributed to the positive electrode. Later, Petibon et al. showed that the increase of impedance in NMC442-graphite cells operated at high cutoff potentials, indeed stems from the positive electrode, proven by using symmetric cells.[45] Even though these results are consistent with our observations on the charge-averaged mean discharge voltage (Figure 1b) one has to be careful since an additive-containing electrolyte was used in
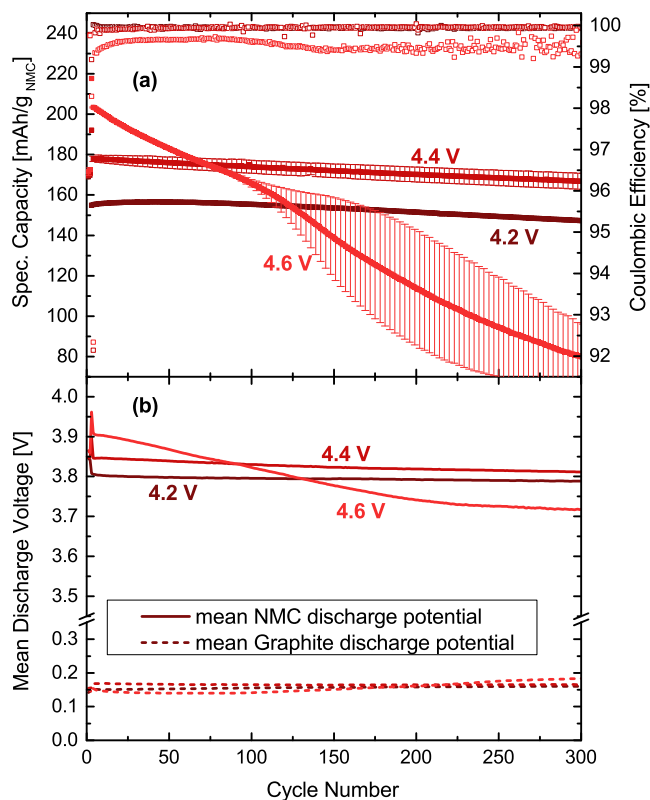
Figure 2. (a) Specific discharge capacity and coulombic efficiency of NMC622-graphite cells and (b) charge-averaged mean discharge voltage (s. Eq. 1) of the NMC622 cathode ($\equiv \bar{V}_{discharge}^{cathode}$; solid lines) and the graphite anode ($\equiv \bar{V}_{discharge}^{anode}$; dashed lines) vs. cycle number in LP57 electrolyte (1 M LiPF$_6$ in EC:EMC 3:7) operated with different upper cutoff voltages (4.2 V, 4.4 V, 4.6 V) and a constant lower cutoff voltage of 3.0 V. Formation was done at a rate of 0.1 C. Cycling was performed at 1 C and 25°C. For each condition, two independent cells were run and the data in the figure always represent the average of two cells (the error bars in (a) represent the standard deviation between the two cells).

Figure 3. (a) Specific discharge capacity and coulombic efficiency of NMC811-graphite cells and (b) charge-averaged mean discharge voltage (s. Eq. 1) of the NMC811 cathode ($\equiv \bar{V}_{discharge}^{cathode}$; solid lines) and the graphite anode ($\equiv \bar{V}_{discharge}^{anode}$; dashed lines) vs. cycle number in LP57 electrolyte (1 M LiPF$_6$ in EC:EMC 3:7) operated with different upper cutoff voltages (4.0 V, 4.1 V, 4.2 V) and a constant lower cutoff voltage of 3.0 V. Formation was done at a rate of 0.1 C. Cycling was performed at 1 C and 25°C. For each condition, two independent cells were run and the data in the figure always represent the average of two cells (the error bars in (a) represent the standard deviation between the two cells).

References [43–45], which likely causes a different surface film formation and impedance. A detailed discussion about the reason for the rise in the polarization of NMC111 with upper cutoff potential is given in the Discussion section.

Figure 2a shows the cycling stability of NMC622-graphite cells. Similar to the case of the NMC111-graphite cells also NMC622-graphite cells can be cycled stably to upper cutoff voltages of 4.2 V and 4.4 V with excellent coulombic efficiencies of >99.9%, whereas at an upper cutoff potential of 4.6 V, the capacity fades rapidly and the coulombic efficiency decreases to ~99.6% (before the rollover-failure), as was observed for NMC111. In analogy to the cells with NMC111, the occurrence of a rollover-failure[41,42] at 4.6 V cutoff indicates growing polarization and causes the large error bars at high cycle numbers as described above. Also with respect to the mean discharge voltages, NMC622 (s. Figure 2b) is very similar to NMC111: $\bar{V}_{discharge}^{cathode}$ slightly increases with cycle number for 4.2 V cutoff voltage, remains essentially constant for 4.4 V cutoff voltage, and decreases rapidly at 4.6 V cutoff voltage, proving a continuous impedance growth of the cathode active material which causes the rollover-failure; on the other hand, $\bar{V}_{discharge}^{anode}$ remains essentially constant, independent of the cutoff voltage.

Figure 3a displays the cycling performance of LiNi$_{0.8}$Mn$_{0.1}$Co$_{0.1}$O$_2$ (NMC811)-graphite cells. Due to the less stable cycling behavior of NMC811, the upper cutoff voltages were limited to 4.0 V, 4.1 V, and 4.2 V. It can be observed that the NMC811 only performs fairly stable with a coulombic efficiency >99.9%, when the upper cutoff voltage is set to 4.0 V. For cutoff potentials of 4.1 V and 4.2 V, poor cycling
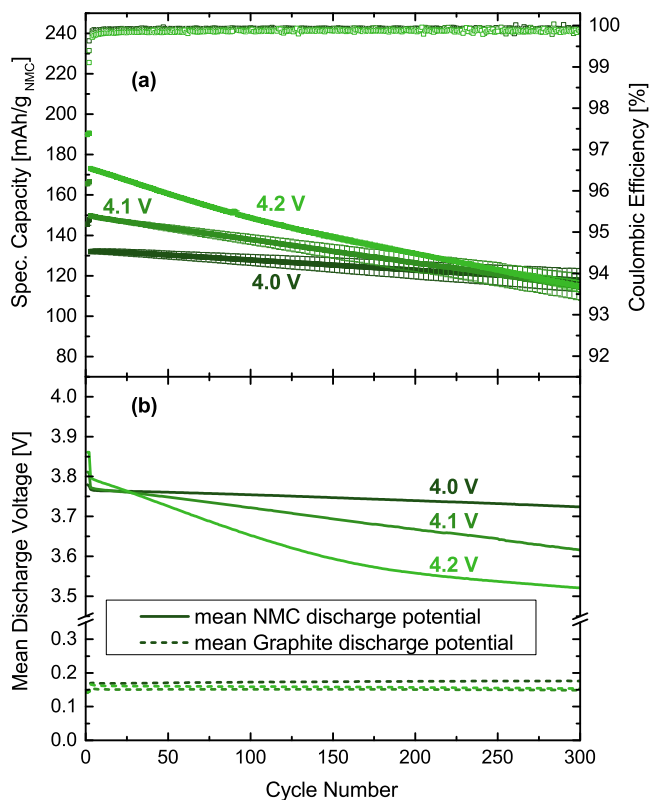
stability is observed. In order to aid the comparison between the different NMCs, the capacity retentions measured between the 5th and the 300th cycles at a 1C-rate for all cells presented in Figures 1–3 are summarized in Table I. Stable cycling with capacity retentions ≥90 % is possible for NMC111 and NMC622 up to 4.4 V and for NMC811 only up to 4.0 V, whereby its capacity retention is still clearly lower than that for the cells with NMC111 and NMC622 cycled to 4.4 V. It is interesting to note that the measured specific capacity of NMC811 at a 4.2 V cutoff is similar to the one of NMC622 at 4.4 V (see values in parentheses in Table I), however, with the latter one still having a stable cycling performance. The impact of the different cutoff voltages on the specific energy of the cells will be picked-up again in the Discussion section. The coulombic efficiencies for the NMC811-graphite cells are >99.9% at 4.0 V cutoff potential, and even at 4.1 V and 4.2 V, where pronounced capacity fading is observed, their coulombic efficiency remains at ~99.9%, i.e., similar to that of the NMC111 and NMC622 cells at 4.4 V. The fact that the latter display substantially lower capacity fading suggests that its origin must be an enhanced cathode and/or anode impedance growth.

The mean discharge voltages versus cycle number of the NMC811 cathodes and the graphite anodes are shown in Figure 3b. Different from the constant or even slightly increasing $\bar{V}_{discharge}^{cathode}$ values with cycle number observed for NMC111 and NMC622 at 4.2 V cutoff potential, the NMC811 cells display a continuously decreasing $\bar{V}_{discharge}^{cathode}$ value, even at the lowest cutoff potential of 4.0 V. At 4.2 V cutoff, $\bar{V}_{discharge}^{cathode}$ drops as rapidly with cycle number for NMC811 as in the case of

Table I. Measured capacity retentions between the 5th and 300th cycle of the NMC-graphite cells shown in Figures 1–3. The values in brackets are the specific capacities in units of mAh/g$_{NMC}$ of the 5th and the 300th cycles.

	4.0 V	4.1 V	4.2 V	4.4 V	4.6 V
NMC111	-	-	93% (140.2 → 130.0)	94% (162.8 → 153.2)	42% (183.4 → 77.1)
NMC622	-	-	95% (155.4 → 147.3)	94% (177.8 → 166.8)	39% (203.1 → 79.9)
NMC811	90% (131.9 → 118.1)	77% (149.3 → 114.4)	66% (172.5 → 114.7)	-	-

4.6 V for NMC111 and NMC622, indicating that the observed strong cathode impedance growth sets in at ∼0.4 V lower cutoff potentials for NMC811. On the other hand, the mean discharge potentials for the graphite anode in the NMC811-graphite cells ($\overline{V}^{anode}_{discharge}$) behave similarly as for the NMC111 and the NMC622 cells, showing negligible increase with cycle number for all cutoff potentials. In summary, the observed capacity decay at >4.0 V cutoff potential for NMC811 full-cells and at >4.4 V for NMC111 and NMC622 full-cells seems to be largely related to the onset of a strong cathode impedance growth (i.e., a strong fading of $\overline{V}^{cathode}_{discharge}$) above these cutoff potentials.

The above results clearly demonstrate a similarity between NMC111 and NMC622, but a big difference to NMC811 with respect to the onset of the cathode impedance growth. To investigate the origin of this difference and to find the reason for the instability occurring for NMC111 and NMC622 at 4.6 V and for NMC811 at 4.1–4.2 V, a dq/dV plot of the delithiation and lithiation of the three NMC materials in NMC-graphite cells of the 3rd cycle is depicted in Figure 4. The voltage region up to 3.8 V is very similar for all three NMC compositions, with two anodic peaks between 3.4 V and 3.8 V. While the first one originates from the lithium intercalation into the graphite anode, the second one stems from the phase transition from a hexagonal to a monoclinic (H1 → M) lattice of the NMC.[18,46–49] In the region >3.8 V, it becomes very obvious that the dq/dV curve for the NMC811 cell deviates substantially from that of the NMC111 and NMC622 cells. In particular, NMC811 has a small anodic feature at ∼3.95 V and a large anodic peak at ∼4.15 V, both of which are absent for the other NMCs. The first one belongs to the M → H2 phase transition and the latter one corresponds to the H2 → H3 phase transition as was reported before for LiNiO$_2$[46–48] and Ni-rich NMC[18,49] materials. In contrast, for NMCs with Ni-contents <80% the M → H2 and H2 → H3 phase transitions have not been reported. Accordingly, for NMC111 and NMC622 such distinct features are not

observed. However, for NMC622 a broad peak around 4.1 V is visible, which might indicate an M → H2 phase transition. For both NMC111 as well as NMC622, a clear redox peak is observed at 4.6 V, which could correspond, in analogy to NMC811, to a H2 → H3 phase transition or could also indicate an oxygen redox feature, a process which has been suggested for Li$_2$Ru$_{1-y}$Sn$_y$O$_3$[50] and Li$_2$IrO$_3$[51] by Tarascon's group and was investigated theoretically using DFT.[52,53] The vertical dotted lines mark the upper cutoff voltages which were chosen for the cells presented in the Figures 1–3. Note that up to the onset of the H2 → H3 phase transition of NMC811 at >4.0 V and up to the onset of the redox feature at >4.4 V of NMC111 and NMC622, the capacity retention of the materials is very stable. In other words, stable cycling was only possible if the cutoff voltage was below the onset of the last peak in the dq/dV plot. The early onset of the H2 → H3 transition at >4.0 V (NMC811) explains why NMC811 cannot be cycled stably at >4.0 V cutoff voltages, whereas NMC111 and NMC622 cells show an excellent performance at potentials as high as 4.4 V. The detrimental effect of the H2 → H3 phase transition was already described before for LiNiO$_2$ and NMC811 and was explained by a significant reduction of the unit-cell volume upon this phase transition, which we will critically review in the Discussion section.[18,47]

Gas analysis of NMC-Li and LNMO-Li half-cells by OEMS.— Figure 5 shows the results of On-line Electrochemical Mass Spectrometry (OEMS) measurements with NMC-Li and LNMO-Li half-cells. For these experiments, metallic lithium was chosen as a counter-electrode in order to achieve a stable reference potential. Figure 5a displays the voltage profiles of NMC111 (black), NMC622 (red), NMC811 (green) as well as LNMO (blue) upon the first charging from OCV to 5 V at a 0.05 C-rate and 25°C as a function of the state-of-charge (SOC) (note that 100% SOC is defined as the removal of all lithium from the cathode materials; s. Experimental section). The three lower panels show the total moles of evolved gas, normalized to the BET surface area of the cathode active material (CAM) in units of μmol/m$^2_{CAM}$ for O$_2$ (Figure 5b), CO$_2$ (Figure 5c), and CO (Figure 5d). Note that normalization of the gassing data to the BET surface area is meant to account for the differences in the available surface area for electrochemical oxidation reactions. Figure 5b demonstrates that for all three NMC compositions a release of oxygen can be detected near a state-of-charge of ∼80–90%, corresponding to onset potentials for O$_2$ evolution of ∼4.3 V vs. Li/Li$^+$ (or ∼4.2 V cell voltage in a full-cell vs. graphite) for NMC811 and of ∼4.7 V vs. Li/Li$^+$ (or ∼4.6 V cell voltage in a full-cell vs. graphite) for NMC111 and NMC622 (this will be seen more clearly later, when discussing Figure 6). The observed onset for O$_2$ evolution on NMC111 at ∼80% SOC during electrochemical delithiation (s. Figure 5) is in surprisingly good agreement with the observed onset for oxygen loss upon the chemical delithiation of NMC111 (with NO$_2$BF$_4$), which was found to initiate at a lithium content corresponding to ∼75% SOC.[6] The scatter in the reported O$_2$ concentration of ca. ±0.5 μmol$_{O_2}$/m$^2_{CAM}$ for NMC111 and NMC622 and of ca. ±1 μmol$_{O_2}$/m$^2_{CAM}$ for NMC811 corresponds to our experimental error in quantifying the O$_2$ concentration of ca. ±10 ppm. As was already reported previously,[54] no O$_2$ evolution is observed for the LNMO half-cell up to 5.0 V.

At roughly the same potentials at which the evolution of O$_2$ initiates, a strong increase of the CO$_2$ (Figure 5c) and the CO (Figure 5d) evolution rates (i.e., an increase in the slope of the lines) is observed for all NMC materials. Here it should be noted that the more gradual increase of the CO$_2$ concentration (Figure 5c) starting at low SOC
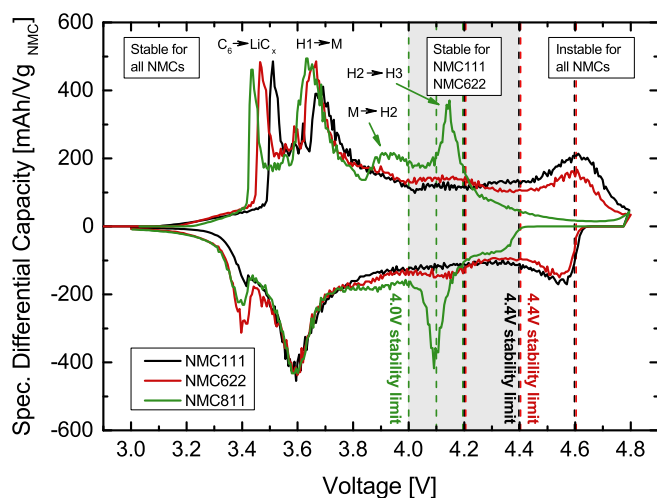

Figure 4. Differential capacity vs. cell voltage of NMC-graphite cells recorded at a 0.1 C-rate (3rd cycle). The vertical dotted lines mark the upper cutoff voltages, which were chosen for the cells in Figures 1–3. The peaks are assigned to their corresponding phase transitions with H1, H2 and H3 representing the three hexagonal phases and M the monoclinic one. C$_6$ → LiC$_x$ indicates the lithiation of graphite.
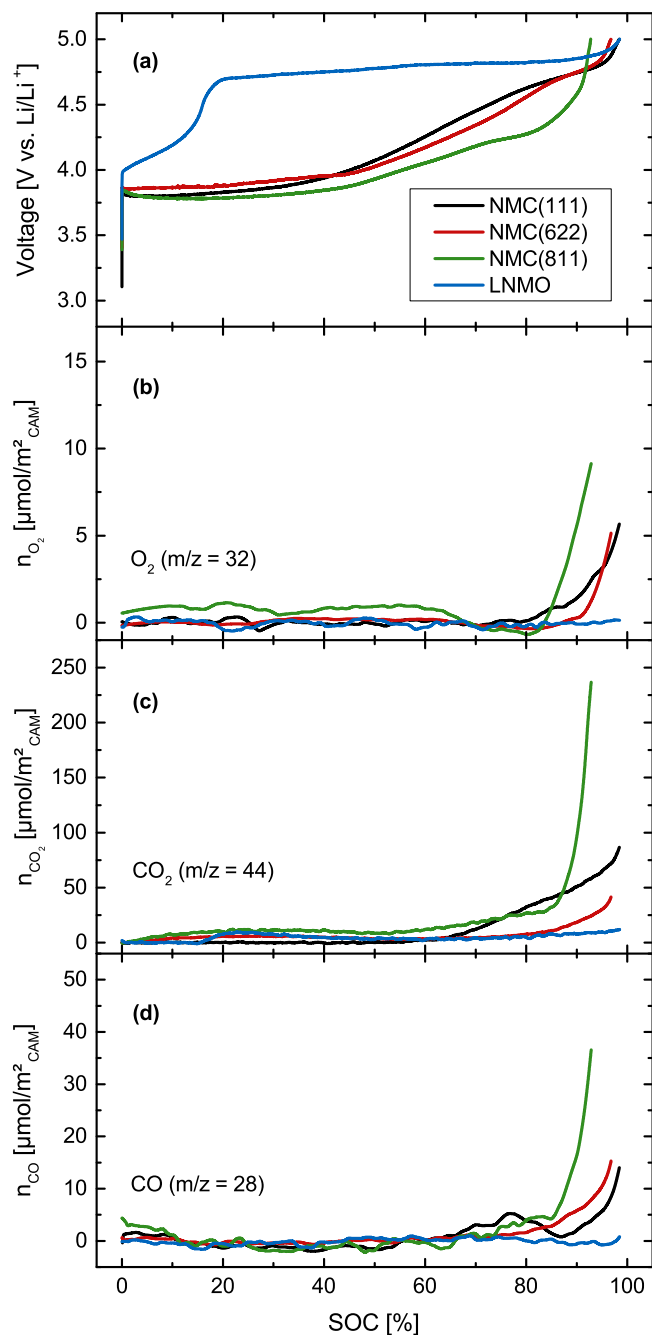
Figure 5. (a) Cell voltage vs. specific capacity of NMC-Li cells using NMC111 (black), NMC622 (red), NMC811 (green), and LNMO (blue). The cells contain 120 μL LP57 electrolyte (1 M $LiPF_6$ in EC:EMC 3:7) and Celgard H2013 separators. The total moles of evolved gases in the OEMS cell, normalized by the cathode active material (CAM) BET area versus the theoretical state-of-charge (SOC) is shown for (b) O_2, (c) CO_2, and (d) CO.
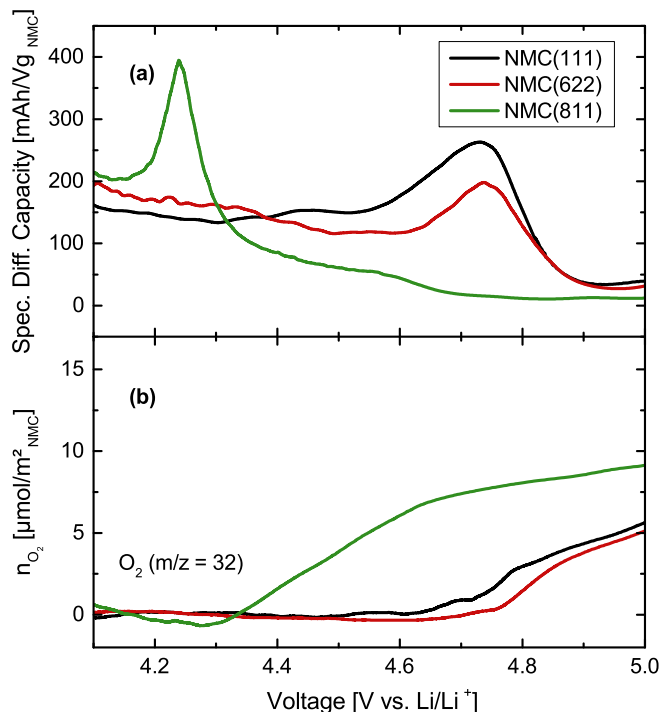

Figure 6. (a) Specific differential capacity vs. cell voltage of the NMC-Li cells shown in Figure 5. (b) Evolution of O_2 as a function of the cell voltage. The OEMS data are smoothed, baseline corrected, and converted into units of $[\mu mol/m^2_{NMC}]$.

values is believed to be due to the electrooxidation of Li_2CO_3 impurities (reported to occur in the potential range above ~3.7 V[55] to ~4.0 V[12]) and possibly of transition metal carbonates in the first charge depicted in Figure 5. In this case, one would expect that the CO_2 evolution at low voltages (i.e., below ~4.2 V) would be absent in the second charge, which indeed is the case (see discussion of Figures 7–9). In addition, the fact that the evolution of CO does not occur until the onset of O_2 evolution (s. Figure 5d) is consistent with the assumption that the CO_2 evolution at lower potentials is due to the oxidation of carbonate impurities. The very similar onsets of O_2, CO_2,

and CO evolution raise the question whether the formation of CO_2 and CO at higher potentials is only due to the electrooxidation of the electrolyte and/or the conductive carbon on the cathode surface, or if it is linked to the release of highly reactive oxygen (e.g., atomic oxygen or singlet oxygen) from the NMC lattice and its subsequent chemical reaction with electrolyte and/or conductive carbon to CO and CO_2. We will present a detailed answer to this fundamental question in the Discussion section, and first present the other experimental results.

Again, in contrast to the data shown for the NMC materials, no CO evolution is observed for the LNMO half-cell up to 5.0 V, and only minor amounts of CO_2 (~10 $\mu mol/m^2_{CAM}$) are formed at ~15% SOC (corresponding to ~4.5 V), which are likely due to the oxidation of low amounts of carbonate impurities on the surface of LNMO. This is at variance with Luo et al.,[35] who observed the formation of CO_2 on LNMO surfaces above 4.75 V (at room temperature), which they suggested to be due to the electrooxidation of electrolyte. While we cannot explain this discrepancy, we do not observe any significant CO/CO_2 formation on LNMO at >4.7 V and up to 5.0 V (i.e., after the initial formation from presumably surface impurities), so that we believe that the electrochemical oxidation of the electrolyte and/or the carbon support is negligible on LNMO surfaces up to 5.0 V at 25°C (this is consistent with our previous OEMS study[54]). The fact that hardly any gas evolution is observed at operating voltages as high as 5 V for LNMO but that significant CO/CO_2 formation is observed for the NMC materials at >4.2 V, supports the hypothesis that the CO and CO_2 evolution is at least partially a consequence of the release of reactive oxygen from the NMC lattice. A catalytic effect of Ni or Co on the electrolyte oxidation also appears unlikely, as the gas evolution for NMC111 and NMC622 shows great similarity, although the materials differ in both the Ni and the Co content. More clearly, a catalytic effect of Ni species can be ruled out due to their presence in LNMO, which evidently shows insignificant gas evolution up to 5.0 V.
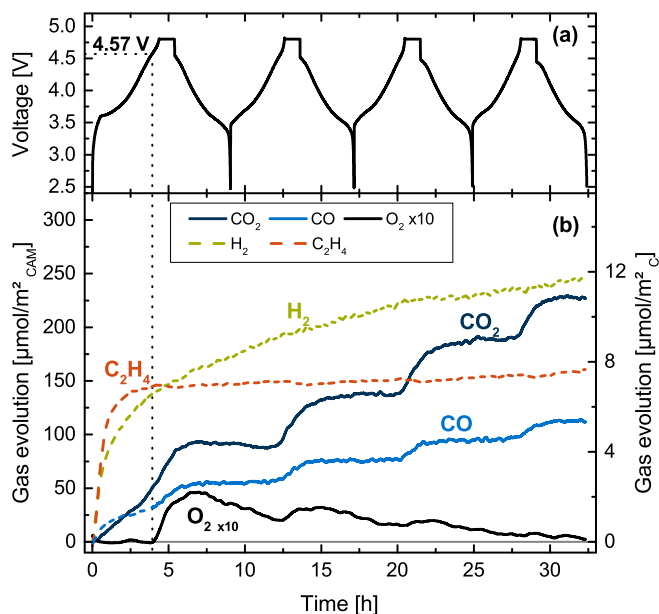
Figure 7. (a) Cell voltage vs. time of a NMC111-graphite cell over four charge/discharge cycles at 0.2 C and 25°C between 2.6 and 4.8 V, in a cell containing 400 μL of 1.5 M $LiPF_6$ in ethylene carbonate (EC), glass-fiber separators and 16.69 mg NMC111. (b) Evolution of CO_2 (dark blue), H_2 (green), C_2H_4 (orange), CO (blue), and O_2 (black, 10-fold magnified) as a function of time. Solid lines indicate the gases stemming from the NMC electrode and dashed lines from the graphite electrode; gas concentrations are referenced to the NMC BET area (left y-axis) and to the sum of graphite and conductive carbon BET area (right x-axis). The OEMS data are smoothed, baseline corrected, and converted into units of $[\mu mol/m^2_{NMC}]$ and $[\mu mol/m^2_C]$.

Figure 8. (a) Cell voltage vs. time of a NMC622-graphite cell over four charge/discharge cycles at 0.2 C and 25°C between 2.6 and 4.8 V, in a cell containing 400 μL of 1.5 M $LiPF_6$ in ethylene carbonate (EC), glassfiber separators and 20.23 mg NMC622. (b) Evolution of CO_2 (dark blue), H_2 (green), C_2H_4 (orange), CO (blue), and O_2 (black, 10-fold magnified) as a function of time. Solid lines indicate the gases stemming from the NMC electrode and dashed lines from the graphite electrode; gas concentrations are referenced to the NMC BET area (left y-axis) and to the sum of graphite and conductive carbon BET area (right x-axis). The OEMS data are smoothed, baseline corrected, and converted into units of $[\mu mol/m^2_{NMC}]$ and $[\mu mol/m^2_C]$.

In order to better visualize the gas evolution at the H2 → H3 phase transition for NMC811 and at the redox feature at ~4.6 V for NMC111 and NMC622, which were shown to be detrimental for the cycling stability, the charging curves of the NMC materials in Figure 5 are now plotted in their dq/dV representation and the corresponding O_2 evolution data are shown as a function of the potential (see Figure 6). The observed peaks in the specific differential capacity vs. voltage plot (Figure 6a) are in good agreement with the features observed in Figure 4 (note that the positive shift of ~0.1 V in the peak positions in Figure 6a is due to the fact that in Figure 4 the full-cell potential is plotted, whereas in Figure 6a the potential is plotted vs. Li). Figure 6b depicts the O_2 evolution and demonstrates clearly that the onset potential of O_2 evolution fits very well to the H2 → H3 phase transition (NMC811) and to the redox feature at ~4.6 V (NMC111 and NMC622), indicating that the release of oxygen is not related to a specific potential, but is rather depending on the occurrence of this very last peak in the dq/dV plot.

Gas analysis of NMC-graphite full-cells by OEMS.—In order to investigate if oxygen release occurs only in the first cycle or also in the subsequent ones, the gas evolution was measured for all three NMC materials cycled four times in a full-cell setup at 0.2 C vs. a graphite anode. In order to avoid signal fluctuations (i.e., on the oxygen channel m/z = 32) coming from the transesterification of the linear carbonate EMC,[40,56–58] the LP57 electrolyte is replaced by 1.5 M $LiPF_6$ in EC for these full-cell experiments. Additionally, due to the low vapor pressure of EC, the background signals from the electrolyte decrease by two orders of magnitude, leading to an improved signal to noise ratio in the mass spectrometer.[59] Since we are particularly interested in the oxygen release occurring at the last peak in the dq/dV plot (see Figure 4 and Figure 6), the upper cutoff potentials were 4.8 V for NMC111 and NMC622, and 4.4 V for NMC811 (compare to features in Figure 4 and Figure 6a). The first four cycles of the NMC111-graphite cell are depicted in Figure 7a
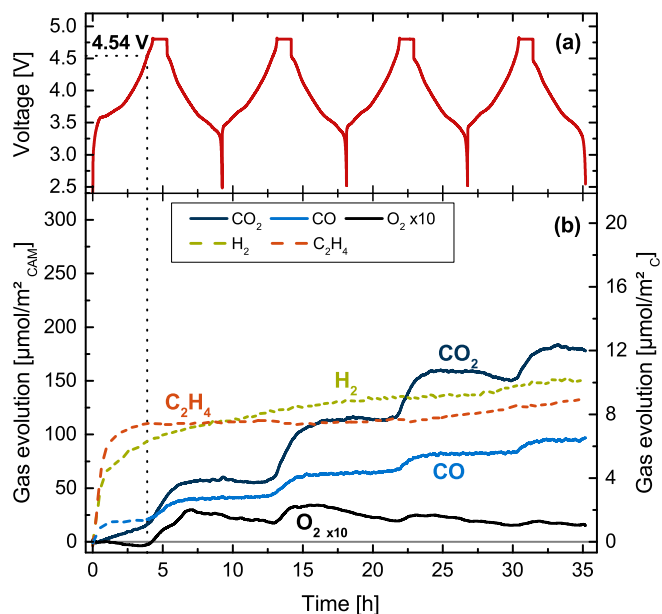
together with the corresponding evolution/consumption of CO_2, H_2, O_2, CO, and C_2H_4 in Figure 7b. From the beginning of the first charge, a steep increase of the ethylene signal (dashed orange line) is observed, which is caused by the reduction of EC in the course of the SEI formation on the graphite electrode.[12,60–62] Once the SEI is formed, the reduction of EC stops, so that the ethylene concentration stays constant at around 8 μmol/m^2_C (s. right-hand y-axis), an amount equal to ~1.2 monolayers of the main EC reduction product lithium ethylene dicarbonate (LEDC) on the graphite anode.[12] Simultaneously with the ethylene evolution, roughly 1.2 μmol/m^2_C carbon monoxide (dashed light-blue line) are evolved (after ca. 2.5 hours), which are typically ascribed to a minor EC reduction pathway with the ring opening at the carbonyl carbon atom.[12,63] Subsequently, the CO signal shows a stepwise increase, which will be discussed in the next paragraph. Furthermore, hydrogen (dashed green line) starts to evolve from the beginning of the measurement, due to the reduction of trace water in the electrolyte.[12,64] The H_2 signal initially evolves at a fast rate and then gradually approaches a concentration of ~12 μmol/m^2_C by the end of the measurement. The reason why the H_2 evolution does not stop after the first charge like the C_2H_4 evolution is, we believe, caused by the formation of protic species from electrolyte decomposition and their subsequent reduction at the graphite anode yielding continuous hydrogen evolution.[12]

Besides C_2H_4, CO, and H_2 one can also observe a linear increase of the CO_2 concentration in the first four hours of the measurement (up to ~4.6 V cell potential) to 50 μmol/m^2_{NMC}. This increase can be assigned to the oxidation of carbonate impurities on the NMC particles, which are typically around 0.1 %$_{wt}$.[12,18] The total CO_2 signal of 50 μmol/m^2_{NMC} corresponds to ~50 μmol/m^2_{NMC} · 0.26 m^2/g · 16.69 mg_{NMC} = 217 nmol CO_2 or to 217 nmol of carbonate (in the case of Li_2CO_3, it was shown, that one mole of Li_2CO_3 releases one mole of CO_2 upon electrochemical oxidation[65]). If referenced to Li_2CO_3 (73.89 g/mol), which is customarily done, this would amount to 16 μg Li_2CO_3 equal to 0.10 %$_{wt}$.
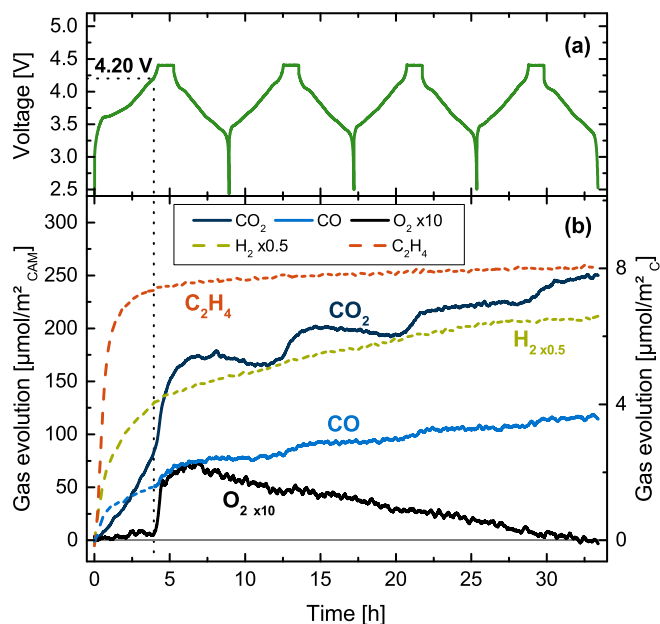
Figure 9. (a) Cell voltage vs. time of a NMC811-Graphite cell over four charge/discharge cycles at 0.2 C and 25°C between 2.6 and 4.4 V, in a cell containing 400 μL of 1.5 M LiPF$_6$ in ethylene carbonate (EC), glassfiber separators and 16.40 mg NMC811. (b) Evolution of CO$_2$ (dark blue), H$_2$ (green), C$_2$H$_4$ (orange), CO (blue), and O$_2$ (black, 10-fold magnified) as a function of time. Solid lines indicate the gases stemming from the NMC electrode and dashed lines from the graphite electrode; gas concentrations are referenced to the NMC BET area (left y-axis) and to the sum of graphite and conductive carbon BET area (right x-axis). The OEMS data are smoothed, baseline corrected, and converted into units of [μmol/m$^2_{NMC}$] and [μmol/m^2_C].

After four hours, the cell voltage reaches ∼4.6 V and oxygen starts to evolve. The onset potential fits very well to the one found in Figure 6 (note that in the Figures 7–9 the NMC–graphite full-cell potential is reported, whereas in Figure 6 the potential is measured vs. a metallic lithium counter electrode, the potential of which is ∼0.1 V below the potential of lithiated graphite). Simultaneously to O$_2$, the CO and CO$_2$ signals increase until the cell switches from the CV-phase at 4.8 V to the discharge, from which point on the CO and CO$_2$ concentrations stay constant until the cell voltage again increases above ∼4.6 V in the following cycles, where O$_2$, CO, and CO$_2$ evolve again, leading to a stepwise increase of these signals. The fact that after the first cycle no CO$_2$ is evolved below ∼4.6 V in any of the subsequent cycles confirms our prior hypothesis that the CO$_2$ evolution below 4.6 V is due to the oxidation of carbonate impurities in the first cycle (s. discussion of Figure 5). By subtracting the amount of CO evolved during the SEI formation (∼1.2 μmol/m^2_C or ∼25 μmol/m$^2_{NMC}$) and the amount of CO$_2$ related to carbonate impurity oxidation in the first cycle (∼50 μmol/m$^2_{NMC}$), the total amount of CO and CO$_2$ evolved exclusively due to processes at high voltage after the four cycles are ∼80 μmol/m$^2_{NMC}$ and ∼180 μmol/m$^2_{NMC}$, respectively.

While the step-like profile of the oxygen signal is similar to that of the CO and CO$_2$ signal, showing a rapid rise every time the potential goes above ∼4.6 V, it does exhibit a superimposed potential-independent continuous decrease. This consumption of oxygen in the cell is most likely caused by a slow but steady reduction of the evolved oxygen at the graphite anode, which would be consistent with the observed decreasing consumption rate over time, as a more protective SEI is being formed (note that an analogous consumption of CO$_2$ is observed in the second and, to a much lesser degree in the third cycle, which appears smaller in magnitude than the O$_2$ consumption only due to the fact that the oxygen signal is magnified by a factor of ten). Thus, in order to estimate the total amount of evolved oxygen over the four cycles, one can sum up the steep increases of the oxygen signal in each cycle, which gives a total oxygen evolution of ∼9 μmol/m$^2_{NMC}$.

Note that all values which are summed up over the four cycles are corrected for the decreasing concentrations due to gas consumption (for CO$_2$ and O$_2$) on the graphite anode by summing up the increases rather than considering the total concentrations measured at the end of the experiment. Additionally, it is quite apparent that the amount of evolved oxygen decreases from cycle to cycle, which would be consistent with our assumption that the oxygen is released mainly from the near-surface regions of the NMC particles and that its release becomes slower as the oxygen depleted surface layer increases in thickness.[36] This hypothesis is also supported by the total amount of released oxygen, which will be discussed in further detail in the Discussion section.

The results of the analogous experiment with an NMC622-graphite cell cycling at 0.2 C between 2.6 V and 4.8 V are shown in Figure 8. For all gases, a very similar trend as for the NMC111-graphite cell is observed. The total amounts of evolved gases during SEI-formation are ∼8 μmol/m^2_C of ethylene and ∼1.2 μmol/m^2_C of CO. Additionally, ∼10 μmol/m^2_C of hydrogen is evolved over the course of the experiment. Prior to the onset of oxygen evolution at ∼4.54 V (vertical dotted line), the oxidation of carbonate impurities results in ∼19 μmol/m$^2_{NMC}$ CO$_2$. This corresponds to ∼19 μmol/m$^2_{NMC}$ · 0.35 m^2/g · 20.23 mg$_{NMC}$ = 135 nmol CO$_2$ or to 135 nmol of carbonate. Again, if referenced to Li$_2$CO$_3$, this would amount to 10 μg Li$_2$CO$_3$ equal to 0.05 %$_{wt}$. As was observed for NMC111, no CO$_2$ is evolved below ∼4.5 V in any of the subsequent cycles, confirming our prior hypothesis that the CO$_2$ evolution below 4.5 V is due to the oxidation of carbonate impurities in the first cycle (s. discussion of Figure 5).

By subtracting the amount of CO evolved during the SEI formation (∼1.2 μmol/m^2_C or ∼20 μmol/m$^2_{NMC}$) and the amount of CO$_2$ related to carbonate impurity oxidation in the first cycle (∼19 μmol/m$^2_{NMC}$), the total amount of CO and CO$_2$ evolved exclusively due to processes at high voltage after the four cycles are ∼79 μmol/m$^2_{NMC}$ and ∼171 μmol/m$^2_{NMC}$, respectively. The estimated amount of evolved oxygen over the four charge/discharge cycles using the above described approach is ∼6 μmol/m$^2_{NMC}$. The total amounts of gaseous species are very similar for both the NMC111-graphite and NMC622-graphite cells, illustrating once again a similarity also in the gassing behavior of NMC111 and NMC622 as it was shown in Figure 5 and Figure 6.

Lastly, a similar experiment was performed with an NMC811-graphite cell (see Figure 9), except that the upper cutoff voltage was reduced to 4.4 V, as this voltage is sufficient to include the complete peak stemming from the H2 → H3 transition (see Figure 4). During the SEI formation a total of ∼8 μmol/m^2_C of ethylene and ∼1.5 μmol/m^2_C of CO are evolved. These amounts fit very well to the gas amounts detected in the experiments with NMC111 and NMC622 (see Figure 7 and Figure 8), which is expected since the gases at this initial stage of the first cycle were shown to originate solely from the graphite electrode,[12] i.e., they are independent of the cathode material. Over the four cycles of the measurement, ∼13 μmol/m^2_C of hydrogen are formed, which also fits to the amounts measured in the NMC111 and NMC622 cells. The upper cutoff potential can have an influence mainly on the hydrogen evolution as a result of the cross-talk between cathode and anode.[12,42,66] The underlying assumption of the following analysis is that the cross-talk effect be either similar for all the measurements or has only a minor effect on the overall gas evolution.

Prior to the onset of oxygen evolution at already ∼4.2 V (vertical dotted line), the oxidation of carbonate impurities results in ∼80 μmol/m$^2_{NMC}$ CO$_2$. This corresponds to ∼80 μmol/m$^2_{NMC}$ · 0.18 m^2/g · 16.40 mg$_{NMC}$ = 236 nmol CO$_2$ (or carbonate). Again, if referenced to Li$_2$CO$_3$, this would amount to 17 μg Li$_2$CO$_3$ equal to 0.11 %$_{wt}$. By subtracting the amount of CO evolved during the SEI formation (∼50 μmol/m$^2_{NMC}$) and the amount of CO$_2$ related to carbonate impurity oxidation in the first cycle (∼80 μmol/m$^2_{NMC}$), the total amount of CO and CO$_2$ evolved exclusively at >4.2 V (i.e., after the onset of oxygen release) after the four cycles are ∼70 μmol/m$^2_{NMC}$ and ∼170 μmol/m$^2_{NMC}$, respectively. The estimated oxygen release over the four cycles is ∼8 μmol/m$^2_{NMC}$. Thus, even though the upper cutoff
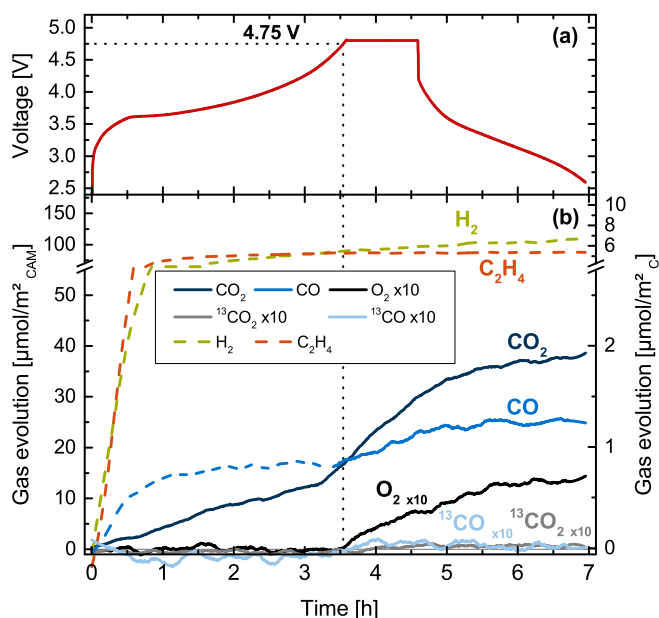
Figure 10. (a) Cell voltage vs. time of a NMC622-graphite cell over the first charge/discharge cycles at 0.2 C and 25°C between 2.6 and 4.8 V, in a cell containing 400 μL of 1.5 M $LiPF_6$ in ethylene carbonate (EC), glassfiber separators and 18.40 mg NMC622. The NMC622 electrode was prepared with ^{13}C-labeled carbon instead of Super C65. (b) Evolution of CO_2 (dark blue), H_2 (green), C_2H_4 (orange), CO (blue), and O_2 (black, 10-fold magnified), [13]CO_2 (gray, 10-fold magnified) and [13]CO (bright blue, 10-fold magnified) as a function of time. Solid lines indicate the gases stemming from the NMC electrode and dashed lines from the graphite electrode; gas concentrations are referenced to the NMC BET area (left y-axis) and to the sum of graphite and conductive carbon BET area (right x-axis). The OEMS data are smoothed, baseline corrected, and converted into units of [μmol/m^2_{NMC}] and [μmol/m^2_C].

potential in the NMC811-graphite cell is reduced by 0.4 V compared to the NMC111 and NMC622 cells, the amounts of evolved CO, CO_2, and O_2 are very similar. This finding is remarkable, because if the CO and CO_2 were a result of electrochemical electrolyte oxidation a difference between the amounts measured at 4.4 V and 4.8 V would be expected, especially since the electrolyte is commonly believed to be stable against oxidation to CO and CO_2 at potentials as low as 4.4 V.[59,67,68] One could explain the similar amounts of gas with 4.4 V (NMC811) and 4.8 V (NMC111 and NMC 622) cutoff potentials, if one were to assume that CO_2 and CO are actually the result of the oxygen release from the NMC lattice. In consequence, this could mean that the electrochemical oxidation of carbonate electrolytes would actually be negligible or at least very low on NMC surfaces at both 4.4 V and even 4.8 V, if there were no release of lattice oxygen, which in turn would explain the complete absence of CO/CO_2 up to 4.8 V in EC-only electrolyte on a carbon black electrode at 25°C.[59] This is also supported by the fact that LNMO can be operated at a potential of 4.8 V with insignificant CO/CO_2 evolution due to the absence of oxygen release (see Figure 5).

Having presented substantial evidence that the CO/CO_2 evolution at high potentials is mostly caused by a chemical reaction of the released lattice oxygen, the question remains whether the evolved CO/CO_2 derive from its reaction with the electrolyte or with the conductive carbon in the NMC electrode. Therefore, an NMC622 electrode with 4.4 %wt ^{13}C-labeled carbon as conductive additive was prepared, replacing the Super C65 conductive carbon, such that a reaction of released lattice oxygen with carbon would result in [13]CO/[13]CO_2, while its reaction with electrolyte would result in [12]CO/[12]CO_2. The NMC622-graphite cell with ^{13}C conductive carbon was charged to 4.8 V and subsequently discharged to 2.6 V (see Figure 10a). The capacity reached during the CC-phase was only 198 mAh/g_{NMC}, i.e., ~17% lower than for the NMC622 electrode with Super C65 (see

Figure 8); this inferior electrode performance is likely caused by the strongly agglomerated structure of the ^{13}C-carbon, resulting in a poor electronic accessibility of the active material particles in the cathode. Nevertheless, also for this electrode, the release of oxygen can be clearly seen. It is shifted to a higher potential of 4.75 V, compared to the 4.54 V for NMC622 with Super C65 (s. Figure 8), which can be rationalized by the fact that the material contains more lithium at ~4.6 V due to the worse cathode performance, which in turn renders it more stable at this voltage. Additionally, the cutoff potential is only 50 mV above the O_2 onset, which is the reason for the overall lower oxygen evolution.

In total, by the end of the first cycle, ~1.5 μmol/m^2_{NMC}, ~23 μmol/m^2_{NMC} and ~9.3 μmol/m^2_{NMC} of O_2, CO_2, and CO were formed, respectively, whereby these values were again corrected by the ~13 μmol/m^2_{NMC} CO_2 stemming from carbonate oxidation prior to the onset of oxygen evolution and by the ~1.1 μmol/m^2_C CO originating from EC reduction on the graphite anode. In comparison, in the first cycle of the NMC622-graphite cell with Super C65 (Figure 8) ~2.9 μmol/m^2_{NMC}, ~40 μmol/m^2_{NMC} and ~19 μmol/m^2_{NMC} of O_2, CO_2 and CO were evolved, respectively (again, corrected for contributions from carbonate oxidation and EC reduction). It is interesting to note, that not only the amount of oxygen is cut in half, but also the amounts of CO_2 and CO are cut in half, which shows once more that these gases are linked to the oxygen evolution. Finally, Figure 10 clearly shows that neither the evolution of [13]CO nor [13]CO_2 was observed, proving that the carbon additive in the cathode is stable at potentials of 4.8 V and also stable against the released oxygen from the NMC lattice. Therefore, the observed CO/CO_2 formation at high potentials can be ascribed to the oxidation of EC (possibly also the binder) rather than of the conductive carbon by released lattice oxygen.

Discussion

Correlation between oxygen release and surface structure of NMC.—We first want to focus on the correlation between the H2 → H3 phase transition at ~4.2 V for NMC811 and the high-voltage feature at ~4.6 V of NMC111 and NMC622 observed in the dq/dV analysis (Figure 4) and the oxygen release detected for the different NMCs by OEMS (Figures 7–9). For NMC111 it is known that upon lithium extraction the c-parameter increases until roughly 2/3 of the lithium is removed and it is ascribed to repulsive interactions of the negatively charged oxygen layers upon the removal of the positive lithium ions.[7,11] Upon further removal of lithium, i.e., at higher states of charge, a decreasing c-parameter is reported, which has been linked to increasing covalency between the metal and the oxygen.[7,69] Increasing covalency in principle corresponds to a decrease of the oxygen anion charge density, i.e., an oxidation of the lattice oxygen anions (from 2- in the idealized ionic structure to a lower charge density of the oxygen atom). This hypothesized oxidation of the oxygen anions (recently shown by Tarascon's group for the model compounds $Li_2Ru_{1-y}Sn_yO_3$ and Li_2IrO_3)[50,51] would also be consistent with the release of oxygen from the NMC material. The H2 → H3 phase transition was described in the literature for $LiNiO_2$ (LNO), where it occurs at ~4.2 V vs. Li/Li^+ [46–48] and Li et al. showed by in-situ XRD that the c-parameter of the LNO unit cell at low states of charges gradually increases and drastically shrinks at the H2 → H3 phase transition.[47] At roughly the same voltage, this phase transition also occurs for NMC811, as described by Noh et al. and Woo et al.,[18,49] and the associated volume contraction was hypothesized to lead to capacity fading.[18,49] We believe that in analogy to the interpretation in the case of NMC111 the shrinkage of the c-parameter for NMC811 at the H2 → H3 phase transition can be also a result of a decreasing repulsion between the oxygen layers, caused by the oxidation of the oxygen anions, which finally may result in O_2 release. As was reported by Strehle et al. on Li-rich NMC ($Li_{1+x}(Ni,Mn,Co)_{1-x}O_2$), we believe that due to the limited diffusion length of oxygen anions in the bulk NMC particles at 25°C, the oxygen release is limited to the surface-near region yielding a disordered spinel or rock-salt type layer while the bulk structure stays intact.[36]

By a detailed investigation of the dq/dV plot shown in Figure 4, one can observe that the peak assigned to the H2 → H3 phase transition (NMC811) as well as the high-voltage feature (NMC111 and NMC622) are reversible. If these features are at least partially related to oxygen redox, the reversibility of the peak also indicates a reversibility of the oxygen redox upon relithiation. This reversibility is not contradicting the experimentally observed irreversible oxygen loss, since the dq/dV analysis reflects mostly processes in the bulk, where no oxygen loss can occur due to the limited bulk diffusivity of oxygen anions in the layered oxide particle. We believe that the oxygen release would likely occur throughout the entire particle, if the oxygen anion diffusion were fast enough and/or if the NMC particles were small enough. In other words, the NMC structure is thermodynamically unstable at high degrees of delithiation, and only retains its oxygen and its layered bulk structure due to the kinetically hindered oxygen diffusion. This hypothesis is supported by the literature, where it is reported that layered NMC[21,25,27,70,71] and NCA[22,25,26,70] structures in the charged state (low lithium content) are not stable at high temperatures (> 170°C) and decompose under release of oxygen, forming a disordered spinel or rock-salt structure, which are thermodynamically more stable than the layered structure at low lithium contents. In these reports, the oxygen release is a bulk phenomenon due to the significantly faster oxygen anion diffusion at elevated temperatures. Consequently, a complete transformation of the layered structure into the spinel or rock-salt structure is observed.

The limitation of spinel or rock-salt structures to the surface-near regions was already reported before for various layered oxides.[9,28-31] In particular, Muto et al. found for NCA that the rock-salt formation on the surface can be up to 100 nm thick after 500 cycles at 80°C.[30] Jung et al. investigated NMC532 in the voltage range between 3–4.8 V and found a spinel layer thickness of 12–15 nm and a thickness of the rock-salt phase of 2–3 nm after 50 cycles at room temperature.[9] Abraham et al. observed a 35–45 nm thick rock-salt structure on $LiNi_{0.8}Co_{0.2}O_2$ after calendaric aging of a charged electrode at 60°C for 8 weeks.[28] They also stated that the oxygen release was expected to occur from the surface-near region of the material, as their XAS and EELS data showed both that the Ni:O and Co:O ratios were twice as high on the surface compared to the bulk and that the Ni oxidation states on the surface matched NiO whereas in the bulk it matched that of Ni in a layered structure.[28,29] Even though a release of oxygen could not be shown in these reports, it is implicitly required because of the lower oxygen to metal ratios in the spinel and rock-salt phases compared to the layered structure: MO_2 (layered) → M_3O_4 (spinel) → MO (rock-salt) (i.e., metal/oxygen = 1:2 → 3:4 → 1:1).

In Figures 7–9, the amount of released oxygen is largest in the first cycle and decreases in the subsequent cycles. This fits to the hypothesis that the oxygen is released only from surface-near regions and is therefore fastest in the first cycle, and lower in subsequent cycles, since then it has to diffuse through the already formed disordered spinel or rock-salt layer. In summary, a clear correlation can be made between the structural rearrangement of the NMC particle surface and the release of oxygen. Additionally, the spinel or rock-salt surface layer is very likely the cause of the increase in the polarization (represented by a decrease in the charge-averaged mean discharge voltage of the cathode, $\bar{V}_{discharge}^{cathode}$) observed during cycling in the Figures 1–3.

Connection between released O_2 and evolution of CO and CO_2.— The total amount of oxygen released during the four cycles (Figures 7–9) is similar for all three NMCs, ranging from 6–9 $\mu mol/m_{NMC}^2$ (see Table II) and for the chosen upper cutoff potentials there is no apparent correlation with the Ni or Co contents in the NMCs. Furthermore, Table II summarizes the measured amounts of CO_2 and CO within the four cycles shown in Figures 7–9. They are corrected for the CO_2 derived from carbonate oxidation and for the CO originating from EC reduction, such that only gassing processes at high-voltage are regarded. As was already discussed, a closer examination of the 2nd, 3rd, and 4th cycle in Figures 7–9 reveals that CO/CO_2 only evolve once the evolution of O_2 is observed, confirming that CO/CO_2 produced at low potentials in the 1st cycle is indeed due to SEI formation (CO) and

Table II. Total amounts of oxygen, carbon monoxide, and carbon dioxide evolved at high potentials over the first four cycles in the cells shown in the Figures 7–9 (the amounts of CO_2 stemming from oxidation of carbonate impurities as well as the CO originating from EC reduction, both in the first cycle, were subtracted).

		NMC111	NMC622	NMC811
O_2	[$\mu mol/m_{NMC}^2$]	9	6	8
CO	[$\mu mol/m_{NMC}^2$]	80	79	70
CO_2	[$\mu mol/m_{NMC}^2$]	180	171	170

carbonate impurity oxidation (CO_2). This raises the question, whether CO and CO_2 derive from the chemical reaction of the released lattice oxygen with the electrolyte. A significant reaction of the evolved oxygen with conductive carbon can be excluded, since it was shown in Figure 10 that no ^{13}CO and $^{13}CO_2$ was evolved when ^{13}C labeled carbon was used as conductive additive in the NMC electrode instead of conventional carbon (Super C65). Another interesting observation is that in the case of NMC811-graphite cells, O_2, CO, and CO_2 evolve already at ∼4.2 V. At this potential, no gas evolution is observed for the analogous cells with NMC111 (onset of O_2 evolution at ∼4.57 V) or NMC622 (onset of O_2 evolution at ∼4.54 V), so that it is too low to ascribe the evolved gases to the electrochemical oxidation of the electrolyte, which strongly supports our hypothesis that the evolution of O_2, CO, and CO_2 are of the same origin.

The purely electrochemical oxidation of EC-only electrolyte on a carbon electrode, i.e., in the absence of any possible catalytic effect by transition metal surfaces, was studied in a recent report by Metzger et al. by applying a linear sweep voltammetry procedure from OCV up to 5.5 V with a scan rate of 0.2 mV/s.[59] There, the onset of CO_2 and CO evolution was at ∼4.8 V vs. Li/Li$^+$, where the sum of the CO and CO_2-evolution rate was determined to be 0.3 $\mu mol/(m_C^2 \cdot h)$.[59] For comparison, in the NMC111-graphite cell (Figure 7), the total amount of CO and CO_2 produced between 4.6 V and the end of the first cycle is 59 $\mu mol/m_{NMC}^2$ and was detected within 1.5 h, corresponding to an average evolution rate of ∼39 $\mu mol/(m_{NMC}^2 \cdot h)$; if referenced to the total surface area of conductive carbon and NMC in the cell ($0.052 m_C^2$ and $0.0043 m_{NMC}^2$), this equates to ∼3.0 $\mu mol/(m_{NMC+C}^2 \cdot h)$. Comparing both values and excluding any catalytic effect of the active material for the above-described reasons, it becomes clear that the purely electrochemical oxidation of EC can only account for at best ∼10 % of the evolved CO and CO_2.

This estimate shows that the electrochemical electrolyte oxidation occurs to a certain extent at high potentials, consistent with previous reports in the literature, which show that the voltage of the NMC slowly drops during storage via a self-discharge caused by electrochemical electrolyte oxidation.[72-75] However, once the potential is above the threshold voltage for the release of lattice oxygen, the majority of CO and CO_2 generated in cells containing NMC stems from chemical electrolyte oxidation. A detailed discussion of the chemical and electrochemical pathways and their ratios on the total electrolyte oxidation will be presented below.

While the absence of oxygen evolution for the high voltage spinel makes sense, considering that the spinel phase is the stable phase which forms upon oxygen release of the layered material, it is interesting that no CO and CO_2 are evolved with LNMO up to a potential of 5 V (see Figure 5), on a surface for which one would not expect a substantially different catalytic effect (if there is any) for the electrochemical oxidation of electrolyte than for NMC surfaces. This implies that the electrolyte should be very stable (i.e. negligible or very minor electrochemical electrolyte oxidation) at the potentials used for the NMC-graphite cells, further supporting our hypothesis that most of the CO_2 and CO are produced by the chemical reaction of released lattice oxygen with the electrolyte. Here it should be noted that a chemical reaction of oxygen with EC is expected to be only possible at room temperature, if the oxygen is in a reactive form, e.g., as atomic oxygen or singlet oxygen, because EC does not decompose in dry air

at the operating temperatures of a lithium ion battery (i.e. it does not react with triplet oxygen). Furthermore, a catalytic effect of Ni or Co appears unlikely as NMC111 and NMC622 have almost identical gassing behavior despite their different Ni and Co composition, and as Ni is also present in the LNMO, which evidently does not exhibit significant electrolyte oxidation at room temperature up to 5.0 V.

In Figures 7–9, the oxygen evolution stops after some cycles, whereas the formation of CO and CO_2 from cycle to cycle decreases at a much slower rate. We believe that the more quickly decreasing oxygen signal over cycling is due to the very fast chemical reaction of released reactive oxygen with EC, so that oxygen can only be detected as O_2 gas if a larger amount is formed within a short period of time, preventing that all of the released oxygen reacts with the electrolyte to CO_2 and CO (i.e., allowing for the escape of some fraction of the oxygen into the head-space of the OEMS cell). This can be rationalized by considering that once reactive oxygen is released (in the following we assume that the reactive species is $^1O_2$) two different follow-up reactions are possible i) the chemical reaction with EC, and/or ii) the physical quenching of two singlet oxygen molecules forming triplet oxygen ($2 \,^1O_2 \rightarrow 2 \,^3O_2 + h\nu$). The rate of the first reaction can be written as

$$r_1 = k_1 \cdot \left[^1O_2\right] \cdot [EC] \qquad [2]$$

and depends on the product of the concentrations of singlet oxygen $[^1O_2]$ and EC [EC] (first order reaction with respect to singlet oxygen) and determines how much CO_2 and CO are observed. In contrast, the rate of singlet oxygen quenching can be written as:

$$r_2 = k_2 \cdot \left[^1O_2\right]^2 \qquad [3]$$

It depends on the squared concentration of singlet oxygen (second order reaction with respect to singlet oxygen) and determines how much triplet oxygen is detected in the mass spectrometer. The decay constant for $^1O_2$ in propylene carbonate was shown to be $3.3 \cdot 10^4 \text{ s}^{-1}$,[76] which we assume to be reasonably similar for ethylene carbonate. Additionally, Kazakov et al.[77] proved that both chemical as well as physical quenching occur in acetone, for which decay constants ranging from $2 \cdot 10^4 - 4 \cdot 10^4 \text{ s}^{-1}$ [76] were reported. The similarity of the decay constants led us to expect that also in our system both reactions can occur with the rate constants k_1 and k_2 having similar orders of magnitude, so that the extents of r_1 and r_2 should be mostly dependent on the reactant concentrations $[^1O_2]$ and [EC]. Due to the linear and squared dependency of r_1 and r_2, respectively, on the singlet oxygen concentration, which is fairly low compared to the concentration of EC, it is expected that $r_1 >> r_2$ explaining the much larger quantities of CO_2 and CO, which are roughly 20 times higher than the amount of O_2 (s. Table II). Furthermore, the ratio of r_2/r_1 derived from Reactions 2 and 3 is proportional to the detected ratio of O_2 to CO_2 (assuming that CO_2 is produced by Reaction 2, as discussed later) and can be written as

$$\frac{r_2}{r_1} = \frac{k_2}{k_1 \cdot [EC]} \cdot \left[^1O_2\right] \propto \frac{n(O_2)}{n(CO_2)} \qquad [4]$$

With Eq. 4 it becomes clear that once the release of oxygen becomes slower (due to the growing thickness of the oxygen depleted surface layer), the local concentration of $^1O_2$ decreases, so that the ratio of O_2/CO_2 released to the gas phase (and detected by the mass spectrometer) is predicted to decrease over cycling, as indeed is observed. The gradually decreasing release of lattice oxygen over cycling, which we ascribe to a growing thickness of an oxygen depleted surface layer is also consistent with the observed decrease of the mean discharge potential of the cathode shown in the Figures 1–3. For Li-rich NMC materials ($Li_{1+x}(Ni,Mn,Co)_{1-x}O_2$) the total amount of released lattice oxygen is comparably large in the first cycle.[32–36] For this material class Strehle et al.[36] found a ratio of O_2/CO_2 close to 1/1 in contrast to ~1/20 for the NMC materials (s. Table II), which based on Eq. 4 would suggest a ~20-fold higher $^1O_2$ concentration near the active material surface, surprisingly consistent with the ~20-fold higher BET surface area of the ($Li_{1+x}(Ni, Mn, Co)_{1-x}O_2$) material examined by Strehle et al.[36]

In a recent publication by Li et al. on NMC811 it was suggested that the c-axis contraction of the unit cell at potentials of ~4.2 V may not be the reason for the poor cycling stability.[78] Instead, a rapid increase of the parasitic heat flow above 4.2 V vs. Li/Li+ was detected and it was hypothesized that the highly delithiated cathode surface be very reactive toward the electrolyte causing an increased cathode impedance.[78] Our observation of a growing polarization is consistent with the study by Li et al., however, we believe that it might be the chemical reaction of the released oxygen with the electrolyte that drives the parasitic heat flow, rather than the direct electrochemical oxidation of the electrolyte on the surface. Additionally, Imhof et al. reported CO_2 evolution for LNO already at 4.2 V and ascribed it to the reactivity of the surface toward electrolyte.[79] However, since this onset potential coincides with the H2 → H3 phase transition,[47] we believe that it is more likely related to a release of oxygen from the layered LNO structure, followed by its chemical reaction with the electrolyte to CO_2 rather than to an electrochemical oxidation of the electrolyte at potentials as low as 4.2 V.

In summary, the above discussion strongly supports our hypothesis that the majority of the CO/CO_2 evolution (>90%) during cycling is due to the chemical reaction of released lattice oxygen with the electrolyte, with the exception of the CO/CO_2 evolved at low potentials in the first cycle, which we believe derive from SEI formation (EC reduction on graphite) and carbonate impurity oxidation.

Anode related C_2H_4 and H_2 signals.—The amounts of ethylene evolved in Figures 7–9 are between 7–9 $\mu mol/m_C^2$, very similar to what was observed in a previous report by Metzger et al.[12] In the same report, the hydrogen evolution which was detected from the beginning of the measurement and was ascribed to the reduction of trace water in the electrolyte.[12] The amount of hydrogen accumulated over the four cycles shown in Figures 7–9 ranges from 10–13 $\mu mol/m_C^2$. If we only consider the amount of hydrogen formed in the first cycle before the onset of O_2 evolution (which will lead to further formation of H_2O, as will be discussed later), we find ~6.6 $\mu mol/m_C^2$ H_2 for the NMC111 (Figure 7) and for the NMC622 (Figure 8) cell as well as ~8.0 $\mu mol/m_C^2$ H_2 for the NMC811 cell (Figure 9). The fact that all three values are reasonably similar supports the assumption that the evolution of H_2 up to this point is not related to the cathode active material. With the total surface area of the graphite-electrodes, this corresponds to an absolute amount of ~0.6–0.7 μmol H_2 being evolved. This amount would require 1.2–1.4 μmol H_2O in the electrolyte, if all H_2 were formed via $H_2O + e^- \rightarrow 0.5 \, H_2 + OH^-$. Using the density of the electrolyte (1.5 g/mL)[80] and the electrolyte volume (400 μL), the above amount would correspond to a water content of 36–42 ppm for all three cells, which fits very well with the report by Metzger et al., who observed a hydrogen evolution corresponding to 33 ppm of trace water using an LP57 electrolyte.[12] In summary, the gases from the anode side are consistent with our previous findings.

Proposed mechanism of EC oxidation by reactive oxygen.—As discussed above, our data indicate that the majority of the evolved CO and CO_2 are actually a consequence of the reaction of the released oxygen from the NMC, which is likely very reactive in the moment it is released from the material (see Figures 7–9). In Figure 10, we demonstrated that the carbon source for the CO and CO_2 formation is not the conductive carbon in the electrode. The only remaining carbon source in the cell is therefore ethylene carbonate (EC) and possibly the binder. In Scheme 1, we propose a mechanism for how oxygen might react with EC, whereby it is clear that oxygen in its triplet ground state does not react with EC. As the reaction requires the oxygen to be reduced, there are only the two carbon atoms bound to the hydrogen which can be potentially oxidized (the carbonyl-carbon is already in its maximum oxidation state). Our proposed mechanism starts with an electrophilic attack on the carbon by the O_2 molecule, yielding a peroxo group carrying the proton which was initially bound to the carbon. The rather unstable peroxo group would immediately decompose, forming a carbonyl group and releasing a water molecule. This molecule could potentially decompose forming
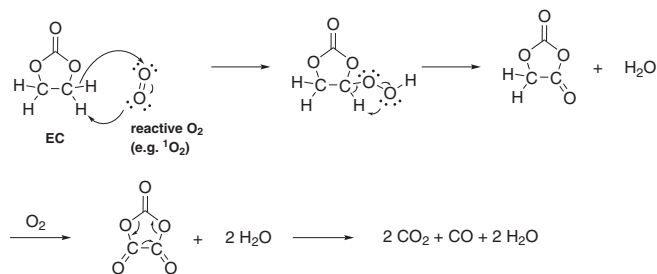
Scheme 1. Proposed mechanism for the oxidation of ethylene carbonate (EC) with reactive oxygen (e.g., singlet oxygen) released from the NMC structure and yielding CO_2, CO, and H_2O. The overall reaction equation is $EC + 2 O_2 \rightarrow 2 CO_2 + CO + 2 H_2O$.

CO, CO_2 and formaldehyde, in which case, however, the predicted CO_2/CO ratio would be 1/1, which does not match the observed ratios in Figures 7—9 nor did we observe any formaldehyde in the mass spectrometer. Instead, a second $^1O_2$ molecule could attack the other carbon atom if the EC molecule attacked in the first step is assumed to be adsorbed at the NMC surface forming another carbonyl group and releasing another molecule of water. The formed molecule would readily decompose, yielding two molecules of CO_2, one molecule CO, aside with the previously formed two H_2O molecules. The formation of water upon the reaction of electrolyte with oxygen was already hypothesized before.[81,82]
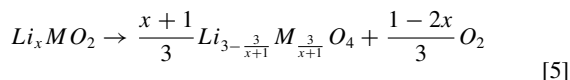
The overall proposed reaction would thus be $EC + 2 O_2 \rightarrow 2 CO_2 + CO + 2 H_2O$, predicting a CO_2 to CO ratio of 2:1. Examining the evolved amounts summarized in Table II, a somewhat higher CO_2:CO ratio ranging from 2.2:1 to 2.4:1 was measured. Considering that water is a reaction product, several follow-up reactions are likely to occur: i) H_2O can be reduced at the graphite anode, yielding H_2 and OH^-, as was reported previously by our group[64] and which would be consistent with the observed continuous evolution of H_2 in Figures 7–9; ii) OH^- produced by the reduction of H_2O at the anode was shown to lead to rather high rates of EC hydrolysis, producing CO_2 gas;[80] iii) chemical reaction of $LiPF_6$ with H_2O can yield $Li_xPO_yF_z$ species, which are frequently reported as surface species at the interface between electrolyte and the NMC cathode.[15,16] A combination of i) and ii) would lead to additional CO_2 evolution (as well as to the observed ongoing H_2 evolution) and therefore to a higher CO_2:CO ratio than the ratio of 2:1 predicted by Scheme 1, consistent with our observations (s. Table II). In order to check if the reduction of water forming H_2 and OH^- can be a reasonable, we will calculate the total amount of water which can be formed according to Scheme 1 and compare it to the H_2 formed at potentials $\geq$ 4.6 V in Figures 7–9. For the following calculation, we will use the values obtained for the NMC111-graphite cell as an example. As stated in Table II, $\sim$80 $\mu mol/m^2_{NMC}$ CO are formed. Assuming the stoichiometry in Scheme 1, this would imply that $\sim$160 $\mu mol/m^2_{NMC}$ H_2O be formed at the same time. Multiplying this value with the active material mass of the NMC electrode (16.69 mg) and the BET-surface area of the NMC111 (0.26 m^2/g), one obtains a total of 0.7 μmol H_2O ($\equiv$ 12.5 μg_{H_2O}). Analogous to the calculation in the previous section, this would correspond to an increase of the H_2O content in the electrolyte by 21 ppm. The reduction of this in-situ formed water at the negative graphite electrode via $H_2O + e^- \rightarrow 0.5 H_2 + OH^-$ could yield 0.35 μmol_{H_2} which, when normalized to the NMC or carbon surface area would amount to 80 $\mu mol/m^2_{NMC}$ and 3.8 $\mu mol/m^2_C$, respectively. Since water can be formed as soon as oxygen is released for the first time, we examine the hydrogen signal in Figure 7 from this point until the end of the measurement: the amount of H_2 increases from 6.6 $\mu mol/m^2_C$ to 11.7 $\mu mol/m^2_C$, i.e., by 5.1 $\mu mol/m^2_C$, which may be compared to the above predicted value of 3.8 $\mu mol/m^2_C$. Analogous estimates can be made for the NMC622 and the NMC811 cells, for which the agreement is also within a factor of $\sim$2. Considering that besides the reduction of the formed water several additional reactions occur simultaneously

Table III. Electrode loading, moles of NMC, theoretically possible amounts of released oxygen and detected amounts of O_2, CO, and CO_2 of the cells shown in Figure 7–9 (the amounts of CO and CO_2 are corrected for the amounts originating from EC reduction and carbonate impurity oxidation). Based on these values, the equations in the text and assuming a layered to spinel or layered to rock-salt transformation the volume fractions (f_{spinel}, $f_{rock-salt}$) from which oxygen is released as well as the oxygen depleted surface layer thicknesses (t_{spinel}, $t_{rock-salt}$) are calculated considering either the sum of O_2 and twice the amount of CO (model I) or the sum of O_2 and CO_2 (model II) according to Scheme 1.
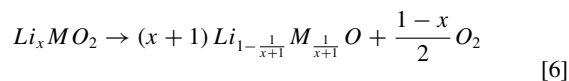
		NMC111	NMC622	NMC811
electrode loading	[mg_{NMC}/cm^2]	9.44	11.45	9.28
amount of NMC	[μmol]	173	209	169
max. $O_{2,spinel}$	[μmol]	51	59	42
max. $O_{2,rock-salt}$	[μmol]	81	96	74
detected O_2	[nmol]	39	42	24
detected CO	[nmol]	347	559	207
detected CO_2	[nmol]	781	1211	502
$f_{spinel,O_2,CO}$ (model I)	[%]	1.4	2.0	1.0
f_{spinel,O_2,CO_2} (model II)	[%]	1.6	2.1	1.3
$f_{rock-salt,O_2,CO}$ (model I)	[%]	0.9	1.2	0.6
$f_{rock-salt,O_2,CO_2}$ (model II)	[%]	1.0	1.3	0.7
$t_{spinel,O_2,CO}$ (model I)	[nm]	11.6	11.8	12.1
t_{spinel,O_2,CO_2} (model II)	[nm]	13.0	12.7	14.6
$t_{rock-salt,O_2,CO}$ (model I)	[nm]	7.3	7.2	6.9
$t_{rock-salt,O_2,CO_2}$ (model II)	[nm]	8.1	7.8	8.2

like hydrogen formation from initially present trace water reduction (see Results section), hydrolysis of EC, as well as decomposition of $LiPF_6$, the calculated maximum of hydrogen from the reduction of in-situ generated water actually fits astonishingly well to the experimentally observed amount.

Estimation of oxygen depleted surface layer thickness.—Based on the OEMS data presented in Figures 7–9 and summarized in Table III, the oxygen depleted surface layer thickness was estimated as a compact, homogeneous layer around the NMC particles in a similar way as reported by Strehle et al.[36] We considered both scenarios, a layered to disordered spinel (Eq. 5) and a layered to rock-salt (Eq. 6) transformation using, in analogy to the literature,[21,22,36,83] the following general equations with M = (Ni, Mn, Co):
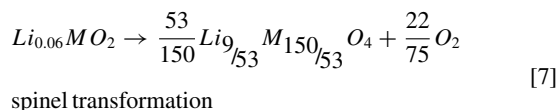
$$Li_x MO_2 \rightarrow \frac{x+1}{3} Li_{3-\frac{3}{x+1}} M_{\frac{3}{x+1}} O_4 + \frac{1-2x}{3} O_2 \qquad [5]$$

spinel transformation

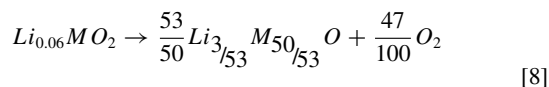$$Li_x MO_2 \rightarrow (x+1) Li_{1-\frac{1}{x+1}} M_{\frac{1}{x+1}} O + \frac{1-x}{2} O_2 \qquad [6]$$

rock-salt transformation

For the x-values in Eqs. 5 and 6 we determined the lithium content in the material at the end of the first charge from Figures 7–9 resulting in x = 0.06, 0.08 and 0.13 for NMC111, NMC622, and NMC811, respectively. Using these x-values the theoretical oxygen loss per mol of NMC can be calculated for the different NMCs:

NMC111:

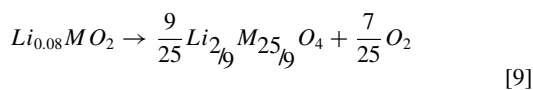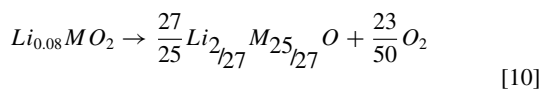$$Li_{0.06}MO_2 \rightarrow \frac{53}{150} Li_{9/53} M_{150/53} O_4 + \frac{22}{75} O_2 \qquad [7]$$

spinel transformation

$$Li_{0.06}MO_2 \rightarrow \frac{53}{50} Li_{3/53} M_{50/53} O + \frac{47}{100} O_2 \qquad [8]$$

rock-salt transformation

NMC622:

$$Li_{0.08}MO_2 \rightarrow \frac{9}{25}Li_{2/9}M_{25/9}O_4 + \frac{7}{25}O_2$$

[9]

spinel transformation

$$Li_{0.08}MO_2 \rightarrow \frac{27}{25}Li_{2/27}M_{25/27}O + \frac{23}{50}O_2$$

[10]

rock-salt transformation

NMC811:

$$Li_{0.13}MO_2 \rightarrow \frac{113}{300}Li_{39/113}M_{300/113}O_4 + \frac{37}{150}O_2$$

[11]

spinel transformation

$$Li_{0.13}MO_2 \rightarrow \frac{113}{100}Li_{13/113}M_{100/113}O + \frac{87}{200}O_2$$

[12]
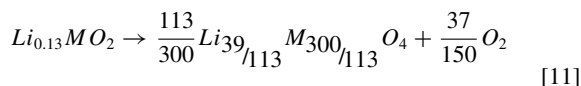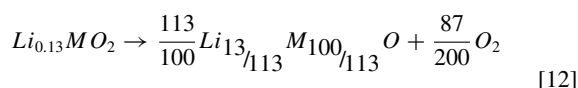
rock-salt transformation

The active material loadings of the electrodes used in the OEMS measurements in Figures 7–9 are listed in Table III. Multiplying by the area (1.767 cm^2) and dividing by the molar mass of the NMC materials yields the amount of NMC in mol (see second row in Table III). Using the stoichiometric relation between the layered oxide on the left-hand-side and the evolved oxygen on the right-hand-side in Eqs. 7–12, the maximum amounts of oxygen which can be evolved if a spinel or rock-salt phase is formed (max. O$_{2, spinel}$ and max. O$_{2, rock-salt}$) can be calculated (see 3rd and 4th row in Table III). For the calculation of the layer thickness from our experimental data we use two different models based on the mechanism presented in Scheme 1. In model I we calculate the layer thickness for the spinel and rock-salt phase taking into account the sum of the detected oxygen plus twice the amount of CO (remember that one mol of CO is formed per two moles of released oxygen in Scheme 1). In contrast, model II is based on the measured amounts of O$_2$ and CO$_2$ (one mol of CO$_2$ is formed per mol of released oxygen). In an ideal case, i.e., if the ratio of CO$_2$/CO were exactly 2:1, both models would yield exactly the same results. As the measured CO$_2$/CO ratio is between 2.2:1 and 2.4:1 due to possible side reactions of the in-situ formed H$_2$O with EC yielding CO$_2$, the calculation with model II will slightly overestimate the layer thickness and can therefore be considered as an upper limit, whereas we believe that model I should yield the more precise values. The detected amounts of O$_2$, CO, and CO$_2$ are given in the 5th-7th row of Table III.

The molar fraction of cathode active material converted to a spinel (f$_{spinel}$) or rock-salt structure (f$_{rock-salt}$) was calculated by dividing either the detected O$_2$ plus twice the amount of detected CO (model I) or the measured amounts of O$_2$ and CO$_2$ (model II) by max. O$_{2,spinel}$ or max. O$_{2,rock-salt}$ (Table III, 8th to 11th row).

The thus estimated molar fractions should be equal to the ratio of the particle shell volume from which oxygen is released (V$_{shell}$) to the total particle volume (V$_{particle}$). Using Eq. 13 and the radius r$_1$ of the complete particle, one can calculate the radius r$_2$ of the intact fraction of the particle. The difference of r$_1$ and r$_2$ is the averaged surface-near layer thickness (t$_{spinel}$, t$_{rock-salt}$) of the oxygen depleted surface layer.

$$\frac{V_{shell}}{V_{particle}} = \frac{4/3\pi\left(r_1^3 - r_2^3\right)}{4/3\pi r_1^3} = 1 - \frac{r_2^3}{r_1^3}$$

[13]

The particle radius r$_1$ was obtained from the respective BET-surface area assuming spherical particles (Eq. 14) and a crystallographic density of NMC of $\rho_{NMC} = 4.8$ g/cm^3.

$$r_1 = \frac{3}{A_{BET} * \rho_{NMC}}$$

[14]

The resulting layer thicknesses for the spinel and rock-salt transformations (t$_{spinel,O_2,CO}$, t$_{spinel,O_2,CO_2}$, t$_{rock-salt,O_2,CO}$, t$_{rock-salt,O_2,CO_2}$) are shown in the 12th-15th row of Table III.

The calculated oxygen depleted volume fractions considering a spinel or rock-salt transformation are in the range 1.0% – 2.1% and 0.6% – 1.3%, respectively. It is interesting to note that the oxygen depleted volume fractions calculated for NMC622 are roughly doubled compared to the ones for NMC811, while the values for NMC111 are in between the two values. Interestingly, this parallels their BET surface area, with the one of NMC111 (0.26 m^2/g) being in between the ones of NMC622 (0.35 m^2/g) and NMC811 (0.18 m^2/g), the latter two being different by a factor of 2. This already suggests that the conversion of the layered to the spinel/rock-salt structure may be limited by the formed oxygen-depleted surface-near film.

Due to the differences in the BET surface area of the three NMCs, the obtained layer thicknesses turn out to be very similar. For model I, the calculated layer thicknesses for the spinel and rock-salt transformations are 11.6 nm–12.1 nm and 6.9 nm–7.3 nm, respectively. Also for the calculation based on model II, the obtained values are very close to the ones obtained using model I (12.7 nm–14.6 nm and 7.8 nm–8.2 nm, respectively). These calculated layer thicknesses are in good agreement with previous reports in the literature on NMC,[9] LiNi$_{0.8}$Co$_{0.2}$O$_2$[28], NCA[30] and Li-rich NMC.[36] As expected, a transformation to the spinel phase leads to a thicker surface layer than the transformation to the rock-salt phase, since the former contains more oxygen in its structure than the latter. Moreover, it is very likely that for the different NMC materials different ratios of spinel and rock-salt phases occur with higher rock-salt ratios for Ni-richer NMC as they tend to form rock-salt rather than spinel phases.[9,70] However, this would not significantly affect the estimated surface layer thickness, as shown in Table III. Additionally, as it was shown in Figures 7–9, an increase in the oxygen signal cannot be observed anymore after a few cycles; however, we believe that the oxygen release is ongoing also in subsequent cycles, but is only detected as CO and CO$_2$. This would also explain the steady decrease of the charge-averaged mean cathode discharge potential shown in Figures 1–3 (solid lines in panels b). All in all, we demonstrated in this section that the film thicknesses deduced from the gas evolution data from OEMS yield values which are consistent with microscopy data from the literature.

Potential dependence of electrochemical and chemical electrolyte oxidation.—In the sections above we showed that the release of reactive oxygen from the surface of the NMC is accompanied by the majority of the observed CO$_2$ and CO evolution (see Figures 7–9). In this section we want to schematically illustrate the relation between electrochemical and chemical electrolyte oxidation, taking into account the results of this work and previous reports in the literature. Scheme 2a depicts the here proposed electrochemical and chemical pathways, exemplified for the oxidation of the commonly used electrolyte constituent EC (analogous mechanisms can be envisioned for other solvents).

The purely electrochemical pathway (see upper left panel in Scheme 2a) sets in when the voltage of the cathode is raised above the stability limit of the electrolyte V$_{solvent\ oxidation}$ which can occur on the surface in contact with the electrolyte (e.g., on conductive carbon additive[59]), at a rate which increases with increasing cathode potential (Scheme 2b). In this process, EC is electro-oxidized to CO or CO$_2$ and protic species (R-H$^+$)[12] which increase the acidity of the electrolyte[84] whereby the in parallel occurring reduction of the protic species on the graphite anode leads to the observed strongly enhanced hydrogen evolution (see Figures 7–9). To compensate the negative charge transferred to the NMC electrode upon electrochemical solvent oxidation, Li$^+$-ions from the electrolyte have to be intercalated into the NMC active material. As a consequence, when storing a battery cell charged to a high cutoff voltage, the electrochemical solvent oxidation and the concomitant Li$^+$ intercalation induce an apparent self-discharge, which can be observed by a voltage drop due to the sloped voltage profile of NMC (s. upper right panel of Scheme 2a).[72–75] Note that during cycling instead of the intercalation of Li$^+$ into the NMC the
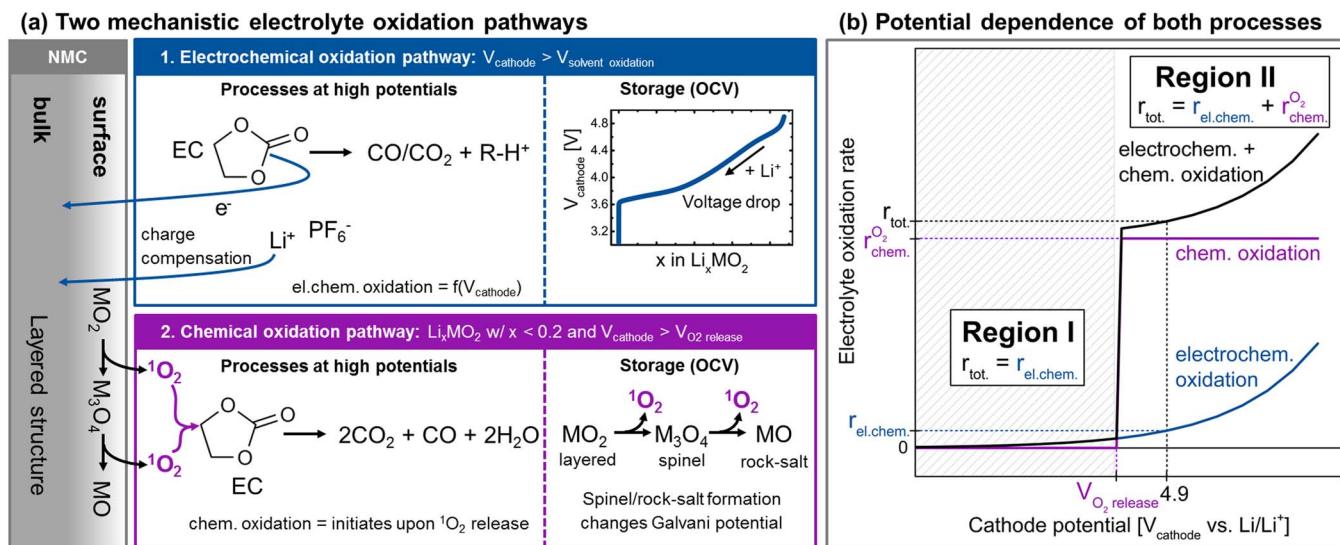
Scheme 2. (a) Schematic description of the proposed electrochemical and chemical electrolyte oxidation pathways (exemplarily shown for EC) which occur at high potentials, and their effect upon battery storage at high potentials. The shown electrochemical EC oxidation yields CO/CO_2 and protic $R\text{-}H^+$ species, and its rate increases with the cathode potential (upper left panel). The intercalation of Li^+ upon electrochemical EC oxidation causes a voltage drop during storage (upper right panel). The chemical EC oxidation initiates upon reactive oxygen release (e.g., singlet oxygen, $^1O_2$) from the NMC surface, which reacts with EC to CO_2, CO, and H_2O (lower left panel). During storage at OCV the surface reconstruction continues as long as the cathode potential is high enough to allow for oxygen release, which is expected to alter the Galvani potential (lower right panel). (b) Schematic potential dependence of both processes: for $V_{cathode} < V_{O_2\ release}$ (Region I), electrolyte oxidation only proceeds via the electrochemical pathway at the rate $r_{el.chem}$ (dark blue line; shown for electrolyte oxidation on conductive carbon[59]); for $V_{cathode} > V_{O_2\ release}$ (Region II), electrolyte oxidation proceeds simultaneously via both the chemical pathway at the rate r_{chem}^{O2} (purple line) and the electrochemical pathways. The sum of both reactions, $r_{tot.}$, is represented by the black line.

electrons can be transferred via the external circuit to the negative electrode and Li^+ would be intercalated into the graphite anode.

In contrast, the here proposed chemical electrolyte oxidation (lower left panel of Scheme 2a) initiates once the cathode potential exceeds the threshold voltage $V_{O_2\ release}$ for the release of reactive oxygen from the layered NMC structure (here depicted exemplarily as singlet oxygen, $^1O_2$). We showed that this surface transformation into a spinel or rock-salt phase occurs at very low lithium contents ($x < 0.2$ in Li_xMO_2) and that the threshold potential $V_{O_2\ release}$ varies for different NMC compositions, being $\sim$4.7 V vs. Li/Li$^+$ for NMC111 and NMC622, and $\sim$4.3 V vs. Li/Li$^+$ for NMC811. The rate of the chemical electrolyte oxidation associated with the release of reactive oxygen (accompanied by the evolution of CO_2 and CO, see Figures 7–9) is hardly potential dependent, i.e., it jumps from quasi zero to a rather high and fairly constant value (see Scheme 2b). Upon OCV storage, the surface reconstruction is ongoing as long as the cathode potential is high enough to allow for it, which is likely to affect the Galvani potential (and thus the OCV) due to the formation of the thermodynamically more stable spinel/rock-salt structure at the near surface layer (lower right panel of Scheme 2a). However, due to the above-described voltage drop during the simultaneously occurring electrochemical electrolyte oxidation (i.e., a gradual re-lithiation of the NMC), the oxygen release will stop as soon as $V_{cathode}$ falls below $V_{O_2\ release}$. Therefore, one would expect that the open circuit potential decay during extended OCV storage is mostly controlled by the rate of the electrochemical pathway.

Scheme 2b schematically summarizes the potential dependence of the electrochemical (dark blue line) and chemical electrolyte oxidation (purple line), with the sum of both processes represented by the black line. As described before, the electrochemical pathway is a function of the cathode voltage, which is shown to proceed at a rate increasing exponentially with potential (dark blue line). In contrast, the chemical pathway is likely to have a very weak potential dependence as long as the released lattice oxygen is provided, which would predict a sudden onset once the potential exceeds $V_{O_2\ release}$ with a weak potential dependence after that point (purple line). At $V_{cathode} < V_{O_2\ release}$ (Region I), no chemical electrolyte oxidation is

expected, so that the total electrolyte oxidation rate (black line) is identical to the electrochemical oxidation (dark blue line). On the other hand, at $V_{cathode} > V_{O_2\ release}$ (Region II), the total electrolyte oxidation rate is the sum of the rates of the electrochemical and chemical pathways, with the latter being the dominant pathway. This implies that the intrinsic electrochemical stability of electrolyte solvents can only be measured with "inert" electrodes which do not release lattice oxygen, e.g., carbon black.[59] Note that the rate of the electrochemical pathway investigated in the report by Metzger et al.[59] at 5.0 V vs. Li/Li$^+$ would only be roughly 10% of the total electrolyte oxidation observed in this work on NMC111 (Figure 7) at 4.9 V vs. Li/Li$^+$ (see second paragraph of the Discussion section for a detailed calculation), which led us to the conclusion that the chemical pathway would be the dominant one at this potential.

In a recent report by Xia et al.,[72] a voltage drop from 4.7 V to roughly 4.5 V was observed for NMC442-graphite cells during storage at OCV for 500 h at 40°C with LP57 electrolyte. A voltage drop by 200 mV in a NMC material corresponds to roughly 20 mAh/g$_{NMC}$, corresponding to an exchanged amount of electrons of 746 μmol$_e$/g$_{NMC}$. As the BET-surface area of the used NMC442 material as well as the electrode composition were not stated, we will assume for the following calculation that its BET surface area was similar to that of our NMC111 (0.26 m^2/g) and that the electrode composition was also similar to that in our study (91.5% NMC and 4.4% C65). Dividing the specific amount of electrons by the estimated surface areas and accounting for the electrode composition, a total of 220 μmol$_e$/m$^2_{NMC+C}$ is obtained. Assuming that the electrochemical oxidation of one solvent molecule leads to the intercalation of one Li^+-ion into NMC, also 220 μmol$_{solvent}$/m$^2_{NMC+C}$ would be decomposed by this process. When dividing this value by the storage time of 500 h, an average decomposition rate of 0.44 μmol$_{solvent}$/(m$^2_{NMC+C}$·h) would be obtained at a potential ranging between 4.8 and 4.6 V vs. Li/Li$^+$. This may be compared with the electrochemical oxidation rate of EC on a carbon surface at 5 V vs. Li/Li$^+$ and 40°C, which was reported to be $\sim$1.1 μmol$_{solvent}$/(m^2_C·h).[59] Thus, the average electrolyte oxidation rate between 4.8 and 4.6 V (vs. Li/Li$^+$) of 0.44 μmol$_{solvent}$/(m$^2_{NMC+C}$·h), which would be required to rationalize the observed potential decay
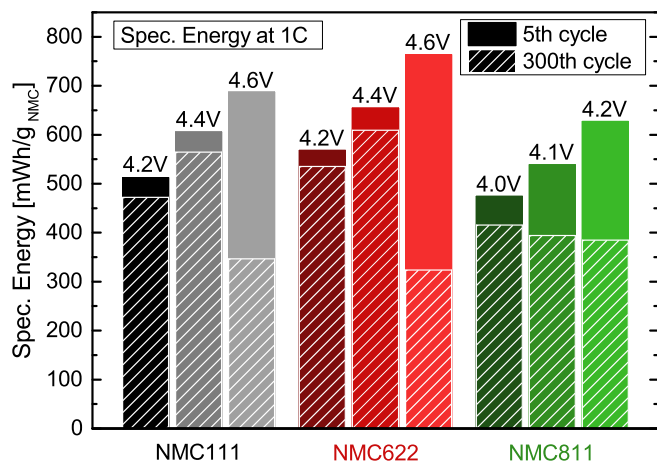
Figure 11. Specific energy of NMC111-graphite, NMC622-graphite and NMC811-graphite cells in LP57 electrolyte (1 M LiPF$_6$ in EC:EMC 3:7). The full columns represent the specific energy of the 5th cycle (1 C-rate), the dashed part of the columns of the 300th cycle (1 C-rate). The data are extracted from the cells shown in the Figures 1–3.

during the OCV hold by Xia et al.[72] is reasonably consistent with the electrochemical EC oxidation rate of ∼1.1 μmol$_{solvent}$/(m$_C^2$·h) at the higher potential of 5.0 V, particularly considering that the EMC oxidation rate in the LP57 electrolyte was found to be even higher (unpublished results). Consequently, we believe that during OCV storage the electrochemical oxidation is the dominating process that leads to the observed voltage drop, as was already stated in the reports by the Dahn group.[72–75] The apparent rate determined in this work, which includes the effect of the chemical electrolyte oxidation due to oxygen release at 25°C and ∼4.9 V vs. Li/Li$^+$ is ∼3.0 μmol$_{solvent}$/(m$_{NMC+C}^2$·h) (see the detailed calculation in the second paragraph of the Discussion section), and is therefore ∼3-fold higher than the rate of pure electrochemical solvent oxidation at higher temperature (40°C) and higher potential (5 V vs. Li/Li$^+$). Compared to the rate of pure electrochemical oxidation at 25°C and 5 V vs. Li/Li$^+$ of ∼0.3 μmol/(m$_C^2$·h) it is even ∼10-fold higher.[59] This unambiguously demonstrates the dominating effect of the chemical electrolyte oxidation at potentials at which oxygen is released from the NMC lattice (Scheme 2b).

Specific energy densities of NMC111, NMC622 and NMC811.— In the previous sections it was demonstrated that the release of oxygen from the NMC surface has a very detrimental impact on the material stability, as it causes significant gas evolution (Figures 7–9) as well as a significant increase of the polarization of the cathode material most probably due to the oxygen depleted surface layer (Figures 1–3). For NMC811, the oxygen release occurs already at potentials as low as 4.3 V vs. Li/Li$^+$, whereas for NMC111 and NMC622 it occurs roughly at 4.7 V vs. Li/Li$^+$. These values limit the end-of-charge voltage that can be applied to achieve a stable cycling and they have therefore a severe impact on the achievable specific energy of these materials. We want to highlight that additional aging mechanisms will be occurring in parallel, like lithium loss due to SEI growth on the anode, electrochemical electrolyte oxidation at high potentials on the cathode, metal dissolution from the cathode, etc.; however, when cycling up to potentials where oxygen release occurs, the formation of a resistive surface layer is the most severe aging mechanism under these conditions, causing significant capacity and discharge voltage fading during extended charge/discharge cycling (Figures 1–3). The specific energies of the cells shown in the Figures 1–3 are depicted in Figure 11 with the full bars representing the specific energy of the 5th cycle at a 1C-rate. The dashed bars indicate the remaining specific energy after 300 cycles. As discussed before, stable cycling was possible for NMC111 and NMC622 up to 4.4 V and up to 4.0 V for NMC811. This is also clearly visible in Figure 11, as the differences between the spe-

cific energies in the 5th and 300th cycle are fairly low for these voltage limits, but increase significantly for the others. The highest specific energy with stable cycling was achieved with NMC622 cycled up to 4.4 V. Comparing only the cells with stable cycling performance, it becomes clear that NMC811 reaches the lowest specific energy, which is due to the very low applicable end-of-charge voltage of only 4.0 V.

This rather sobering outlook for NMC811 emphasizes the need to prohibit the oxygen release from the surface. Our results suggest that one way of making use of the high capacities of NMC811 and achieving stable cycling at the same time might be possible by either a core-shell structure in which the core consists of NMC811 with i) a shell that has a Ni-content of up to 60 % (surface like NMC622) and does not release oxygen until >4.4 V or ii) a shell consisting of an ordered spinel like high-voltage spinel (LNMO) that does hardly evolve any gases (Figure 5) due to the absence of oxygen release. In both cases the shell would need to be thick enough to prevent oxygen loss from the core structure via the limited diffusion of the oxygen anions. Indeed, these approaches have been used by several research groups and we believe that the prevention of oxygen release explains the successful use of core-shell[85–88] materials possessing Ni-contents in the core and shell of 80% and ≤55%, respectively, and full concentration gradient[89–91] materials with Ni-contents of ≥75% and ≤56% in the particle center and the surface, respectively. Additionally, also a superior performance of LiMn$_2$O$_4$ coated NMC over uncoated samples was reported by Cho et al.[92]

Conclusions

This work focused on a fundamental understanding of the aging phenomena at high voltage of LiNi$_{1/3}$Mn$_{1/3}$Co$_{1/3}$O$_2$ (NMC111), LiNi$_{0.6}$Mn$_{0.2}$Co$_{0.2}$O$_2$ (NMC622), and LiNi$_{0.8}$Mn$_{0.1}$Co$_{0.1}$O$_2$ (NMC811). NMC-graphite cells were cycled to different end-of-charge potentials and it was demonstrated that stable cycling is possible up to 4.4 V for NMC111 and NMC622 and only up to 4.0 V for NMC811. The capacity fading rates observed at 4.6 V for NMC111 and NMC622 and 4.1 V and 4.2 V for NMC811 are due to a significant increase in the polarization of the NMC electrode as evidenced by charge/discharge cycling in a 3-electrode setup with a lithium reference electrode. In contrast, the polarization of the graphite electrode remained rather constant. By a dq/dV analysis we demonstrated that the significant rise in the impedance occurs when the NMC materials are cycled up to a high-voltage feature at ∼4.7 V vs. Li/Li$^+$ for NMC111 and NMC622 and up to the H2 → H3 phase transition at ∼4.3 V vs. Li/Li$^+$ for NMC811; we hypothesize that this is caused by oxygen release from the NMC lattice.

Oxygen release is evidenced by On-line Electrochemical Mass Spectrometry (OEMS). Simultaneously with the oxygen evolution, also CO$_2$ and CO are evolved, which we suggest to be mostly due to a chemical reaction of electrolyte with released lattice oxygen rather than the electrochemical oxidation of electrolyte on the cathode surface. We proposed a mechanism for the reaction of released oxygen with ethylene carbonate yielding CO$_2$, CO and H$_2$O. By quantifying the evolved gases, we estimated the thickness of the oxygen depleted surface layer to be up to ∼15 nm, which is in agreement with previous microscopy studies in the literature. Furthermore we showed that no oxygen is released from high voltage spinel (LNMO) and in consequence also no CO$_2$ or CO evolution was observed. These results support the hypothesis that the CO$_2$ and CO evolution at potentials up to 4.8 V is to a large extent linked to the release of oxygen, rather than to the electrochemical oxidation of the carbonate electrolyte.

The highest specific energy of ∼650 mWh/g$_{NMC}$ with a stable cycling performance at a 1 C-rate was obtained in NMC622-graphite cells cycled up to 4.4 V. Due to the low end-of-charge voltage limit of 4.0 V for a stable cycling of NMC811-graphite cells, the achieved specific energy is significantly lower than for the NMC622 cells. Therefore a stabilization of the NMC surface is necessary to prevent the release of oxygen from the particle surface.

References

1. O. Groeger, H. A. Gasteiger, and J. -P. Suchsland, *Journal of The Electrochemical Society*, **162**, A2605 (2015).
2. D. Andre, S. -J. Kim, P. Lamp, S. F. Lux, F. Maglia, O. Paschos, and B. Stiaszny, *J. Mater. Chem. A*, **3**, 6709 (2015).
3. K. G. Gallagher, S. Goebel, T. Greszler, M. Mathias, W. Oelerich, D. Eroglu, and V. Srinivasan, *Energy Environ. Sci.*, **7**, 1555 (2014).
4. I. Belharouak, Y. K. Sun, J. Liu, and K. Amine, *J. Power Sources*, 2003, **123**, 247.
5. M. S. Whittingham, *Chem. Rev. (Washington, DC, U. S.)*, **104**, 4271 (2004).
6. J. Choi and A. Manthiram, *J. Electrochem. Soc.*, **152**, A1714 (2005).
7. N. Yabuuchi, Y. Makimura, and T. Ohzuku, *Journal of The Electrochemical Society*, **154**, A314 (2007).
8. M. G. Kim, H. J. Shin, J. -H. Kim, S. -H. Park, and Y. -K. Sun, *Journal of The Electrochemical Society*, **152**, A1320 (2005).
9. S. -K. Jung, H. Gwon, J. Hong, K. -Y. Park, D. -H. Seo, H. Kim, J. Hyun, W. Yang, and K. Kang, *Adv. Energy Mater.*, **4**, 1300787 (2014).
10. H. Gabrisch, T. Yi, and R. Yazami, *Electrochem. Solid-State Lett.*, **11**, A119 (2008).
11. I. Buchberger, S. Seidlmayer, A. Pokharel, M. Piana, J. Hattendorff, P. Kudejova, R. Gilles, and H. A. Gasteiger, *Journal of The Electrochemical Society*, **162**, A2737 (2015).
12. M. Metzger, B. Strehle, S. Solchenbach, and H. A. Gasteiger, *Journal of The Electrochemical Society*, **163**, A798 (2016).
13. D. R. Gallus, R. Schmitz, R. Wagner, B. Hoffmann, S. Nowak, I. Cekic-Laskovic, R. W. Schmitz, and M. Winter, *Electrochim. Acta*, **134**, 393 (2014).
14. H. Zheng, Q. Sun, G. Liu, X. Song, and V. S. Battaglia, *J. Power Sources*, **207**, 134 (2012).
15. Y. -C. Lu, A. N. Mansour, N. Yabuuchi, and Y. Shao-Horn, *Chemistry of Materials*, **21**, 4408 (2009).
16. A. M. Andersson, D. P. Abraham, R. Haasch, S. MacLaren, J. Liu, and K. Amine, *Journal of The Electrochemical Society*, **149**, A1358 (2002).
17. J. Wandt, A. Freiberg, R. Thomas, Y. Gorlin, A. Siebel, R. Jung, H. A. Gasteiger, and M. Tromp, *Journal of Materials Chemistry A*, **4**, 18300 (2016).
18. H. -J. Noh, S. Youn, C. S. Yoon, and Y. -K. Sun, *J. Power Sources*, **233**, 121 (2013).
19. W. Liu, P. Oh, X. Liu, M. -J. Lee, W. Cho, S. Chae, Y. Kim, and J. Cho, *Angew. Chem., Int. Ed.*, **54**, 4440 (2015).
20. J. Zheng, W. H. Kan, and A. Manthiram, *ACS Appl. Mater. Interfaces*, **7**, 6926 (2015).
21. S. -M. Bak, E. Hu, Y. Zhou, X. Yu, S. D. Senanayake, S. -J. Cho, K. -B. Kim, K. Y. Chung, X. -Q. Yang, and K. -W. Nam, *ACS Appl. Mater. Interfaces*, **6**, 22594 (2014).
22. S. -M. Bak, K. -W. Nam, W. Chang, X. Yu, E. Hu, S. Hwang, E. A. Stach, K. -B. Kim, K. Y. Chung, and X. -Q. Yang, *Chem. Mater.*, **25**, 337 (2013).
23. H. Konishi, T. Yuasa, and M. Yoshikawa, *J. Power Sources*, **196**, 6884 (2011).
24. H. Arai, S. Okada, Y. Sakurai, and J. -i. Yamaki, *Solid State Ionics*, **109**, 295 (1998).
25. I. Belharouak, W. Lu, D. Vissers, and K. Amine, *Electrochemistry Communications*, **8**, 329 (2006).
26. I. Belharouak, D. Vissers, and K. Amine, *Journal of The Electrochemical Society*, **153**, A2030 (2006).
27. S. -T. Myung, K. -S. Lee, C. S. Yoon, Y. -K. Sun, K. Amine, and H. Yashiro, *J. Phys. Chem. C*, **114**, 4710 (2010).
28. D. P. Abraham, R. D. Twesten, M. Balasubramanian, I. Petrov, J. McBreen, and K. Amine, *Electrochem. Commun.*, **4**, 620 (2002).
29. D. P. Abraham, R. D. Twesten, M. Balasubramanian, J. Kropf, D. Fischer, J. McBreen, I. Petrov, and K. Amine, *Journal of The Electrochemical Society*, **150**, A1450 (2003).
30. S. Muto, Y. Sasano, K. Tatsumi, T. Sasaki, K. Horibuchi, Y. Takeuchi, and Y. Ukyo, *Journal of The Electrochemical Society*, **156**, A371 (2009).
31. S. Hwang, W. Chang, S. M. Kim, D. Su, D. H. Kim, J. Y. Lee, K. Y. Chung, and E. A. Stach, *Chem. Mater.*, **26**, 1084 (2014).
32. F. La Mantia, F. Rosciano, N. Tran, and P. Novak, *J. Appl. Electrochem.*, **38**, 893 (2008).
33. P. Lanz, H. Sommer, M. Schulz-Dobrick, and P. Novak, *Electrochim. Acta*, **93**, 114 (2013).
34. A. R. Armstrong, M. Holzapfel, P. Novak, C. S. Johnson, S. -H. Kang, M. M. Thackeray, and P. G. Bruce, *J. Am. Chem. Soc.*, **128**, 8694 (2006).
35. K. Luo, M. R. Roberts, R. Hao, N. Guerrini, D. M. Pickup, Y. -S. Liu, K. Edström, J. Guo, A. V. Chadwick, L. C. Duda, and P. G. Bruce, *Nat Chem*, **8**, 684 (2016).
36. B. Strehle, K. Kleiner, R. Jung, F. Chesneau, M. Mendez, H. A. Gasteiger, and M. Piana, *Journal of The Electrochemical Society*, **164**, A400 (2017).
37. A. Guéguen, D. Streich, M. He, M. Mendez, F. F. Chesneau, P. Novák, and E. J. Berg, *Journal of The Electrochemical Society*, **163**, A1095 (2016).
38. M. Metzger, J. Sicklinger, D. Haering, C. Kavakli, C. Stinner, C. Marino, and H. A. Gasteiger, *Journal of The Electrochemical Society*, **162**, A1227 (2015).
39. N. Tsiouvaras, S. Meini, I. Buchberger, and H. A. Gasteiger, *Journal of The Electrochemical Society*, **160**, A471 (2013).
40. B. Strehle, S. Solchenbach, M. Metzger, K. U. Schwenke, and H. A. Gasteiger, to be submitted.
41. M. Dubarry, C. Truchot, B. Y. Liaw, K. Gering, S. Sazhin, D. Jamison, and C. Michelbacher, *J. Power Sources*, **196**, 10336 (2011).
42. J. C. Burns, A. Kassam, N. N. Sinha, L. E. Downie, L. Solnickova, B. M. Way, and J. R. Dahn, *Journal of The Electrochemical Society*, **160**, A1451 (2013).
43. L. Ma, J. Xia, and J. R. Dahn, *Journal of The Electrochemical Society*, **161**, A2250 (2014).
44. K. J. Nelson, G. L. d'Eon, A. T. B. Wright, L. Ma, J. Xia, and J. R. Dahn, *Journal of The Electrochemical Society*, **162**, A1046 (2015).
45. R. Petibon, L. Madec, D. W. Abarbanel, and J. R. Dahn, *Journal of Power Sources*, **300**, 419 (2015).
46. H. Arai, S. Okada, H. Ohtsuka, M. Ichimura, and J. Yamaki, *Solid State Ionics*, **80**, 261 (1995).
47. W. Li, J. N. Reimers, and J. R. Dahn, *Solid State Ionics*, 1993, **67**, 123.
48. J. P. Peres, F. Weill, and C. Delmas, *Solid State Ionics*, **116**, 19 (1999).
49. S. U. Woo, C. S. Yoon, K. Amine, I. Belharouak, and Y. K. Sun, *J. Electrochem. Soc.*, **154**, A1005 (2007).
50. M. Sathiya, G. Rousse, K. Ramesha, C. P. Laisa, H. Vezin, M. T. Sougrati, M. L. Doublet, D. Foix, D. Gonbeau, W. Walker, A. S. Prakash, M. Ben Hassine, L. DuPont, and J. M. Tarascon, *Nat Mater*, **12**, 827 (2013).
51. E. McCalla, A. M. Abakumov, M. Saubanere, D. Foix, E. J. Berg, G. Rousse, M. -L. Doublet, D. Gonbeau, P. Novak, G. Van Tendeloo, R. Dominko, and J. -M. Tarascon, *Science (Washington, DC, U. S.)*, **350**, 1516 (2015).
52. D. -H. Seo, J. Lee, A. Urban, R. Malik, S. Kang, and G. Ceder, *Nat Chem*, **8**, 692 (2016).
53. M. Saubanere, E. McCalla, J. M. Tarascon, and M. L. Doublet, *Energy & Environmental Science*, **9**, 984 (2016).
54. M. Xu, N. Tsiouvaras, A. Garsuch, H. A. Gasteiger, and B. L. Lucht, *J. Phys. Chem. C*, **118**, 7363 (2014).
55. S. A. Freunberger, Y. Chen, Z. Peng, J. M. Griffin, L. J. Hardwick, F. Bardé, P. Novák, and P. G. Bruce, *Journal of the American Chemical Society*, **133**, 8040 (2011).
56. E. S. Takeuchi, H. Gan, M. Palazzo, R. A. Leising, and S. M. Davis, *Journal of The Electrochemical Society*, **144**, 1944 (1997).
57. H. Yoshida, T. Fukunaga, T. Hazama, M. Terasaki, M. Mizutani, and M. Yamachi, *J. Power Sources*, **68**, 311 (1997).
58. R. Petibon, L. Rotermund, K. J. Nelson, A. S. Gozdz, J. Xia, and J. R. Dahn, *Journal of The Electrochemical Society*, **161**, A1167 (2014).
59. M. Metzger, C. Marino, J. Sicklinger, D. Haering, and H. A. Gasteiger, *Journal of The Electrochemical Society*, **162**, A1123 (2015).
60. B. Zhang, M. Metzger, S. Solchenbach, M. Payne, S. Meini, H. A. Gasteiger, A. Garsuch, and B. L. Lucht, *The Journal of Physical Chemistry C*, **119**, 11337 (2015).
61. M. Nie, D. Chalasani, D. P. Abraham, Y. Chen, A. Bose, and B. L. Lucht, *J. Phys. Chem. C*, **117**, 1257 (2013).
62. D. Aurbach, Y. Gofer, M. Ben-Zion, and P. Aped, *J. Electroanal. Chem.*, **339**, 451 (1992).
63. M. Onuki, S. Kinoshita, Y. Sakata, M. Yanagidate, Y. Otake, M. Ue, and M. Deguchi, *Journal of The Electrochemical Society*, **155**, A794 (2008).
64. R. Bernhard, M. Metzger, and H. A. Gasteiger, *Journal of The Electrochemical Society*, **162**, A1984 (2015).
65. S. Meini, N. Tsiouvaras, K. U. Schwenke, M. Piana, H. Beyer, L. Lange, and H. A. Gasteiger, *Phys. Chem. Chem. Phys.*, **15**, 11478 (2013).
66. R. Dedryvere, D. Foix, S. Franger, S. Patoux, L. Daniel, and D. Gonbeau, *J. Phys. Chem. C*, **114**, 10999 (2010).
67. L. Xing and O. Borodin, *Phys. Chem. Chem. Phys.*, **14**, 12838 (2012).
68. K. Abe, T. Hattori, K. Kawabe, Y. Ushigoe, and H. Yoshitake, *Journal of The Electrochemical Society*, **154**, A810 (2007).
69. Y. Koyama, N. Yabuuchi, I. Tanaka, H. Adachi, and T. Ohzuku, *Journal of The Electrochemical Society*, **151**, A1545 (2004).
70. L. Wu, K. -W. Nam, X. Wang, Y. Zhou, J. -C. Zheng, X. -Q. Yang, and Y. Zhu, *Chem. Mater.*, **23**, 3953 (2011).
71. K. -W. Nam, W. -S. Yoon, and X. -Q. Yang, *J. Power Sources*, **189**, 515 (2009).
72. J. Xia, K. J. Nelson, Z. Lu, and J. R. Dahn, *Journal of Power Sources*, **329**, 387 (2016).
73. J. Xia and J. R. Dahn, *Journal of Power Sources*, **324**, 704 (2016).
74. M. Nie, J. Xia, and J. R. Dahn, *Journal of The Electrochemical Society*, **162**, A1186 (2015).
75. J. Xia, M. Nie, J. C. Burns, A. Xiao, W. M. Lamanna, and J. R. Dahn, *Journal of Power Sources*, **307**, 340 (2016).
76. F. Wilkinson, W. P. Helman, and A. B. Ross, *Journal of Physical and Chemical Reference Data*, **24**, 663 (1995).
77. D. V. Kazakov, V. P. Kazakov, G. Y. Maistrenko, D. V. Mal'zev, and R. Schmidt, *The Journal of Physical Chemistry A*, **111**, 4267 (2007).
78. J. Li, L. E. Downie, L. Ma, W. Qiu, and J. R. Dahn, *Journal of The Electrochemical Society*, **162**, A1401 (2015).
79. R. Imhof and P. Novak, *J. Electrochem. Soc.*, **146**, 1702 (1999).
80. M. Metzger, B. Strehle, S. Solchenbach, and H. A. Gasteiger, *Journal of The Electrochemical Society*, **163**, A1219 (2016).
81. M. Jiang, B. Key, Y. S. Meng, and C. P. Grey, *Chem. Mater.*, **21**, 2733 (2009).
82. S. Meini, S. Solchenbach, M. Piana, and H. A. Gasteiger, *Journal of The Electrochemical Society*, **161**, A1306 (2014).
83. N. Yabuuchi, Y. -T. Kim, H. H. Li, and Y. Shao-Horn, *Chemistry of Materials*, **20**, 4936 (2008).

84. T. Ma, G. -L. Xu, Y. Li, L. Wang, X. He, J. Zheng, J. Liu, M. H. Engelhard, P. Zapol, L. A. Curtiss, J. Jorne, K. Amine, and Z. Chen, *The Journal of Physical Chemistry Letters*, 1072 (2017).
85. J. -Y. Liao and A. Manthiram, *J. Power Sources*, **282**, 429 (2015).
86. Y. -K. Sun, S. -T. Myung, B. -C. Park, J. Prakash, I. Belharouak, and K. Amine, *Nat. Mater.*, **8**, 320 (2009).
87. Y. -K. Sun, S. -T. Myung, M. -H. Kim, J. Prakash, and K. Amine, *J. Am. Chem. Soc.*, **127**, 13411 (2005).

88. Y. -K. Sun, D. -H. Kim, C. S. Yoon, S. -T. Myung, J. Prakash, and K. Amine, *Adv. Funct. Mater.*, **20**, 485 (2010).
89. Y. -K. Sun, Z. Chen, H. -J. Noh, D. -J. Lee, H. -G. Jung, Y. Ren, S. Wang, C. S. Yoon, S. -T. Myung, and K. Amine, *Nat. Mater.*, **11**, 942 (2012).
90. E. -J. Lee, H. -J. Noh, C. S. Yoon, and Y. -K. Sun, *J. Power Sources*, **273**, 663 (2015).
91. C. Hua, K. Du, C. Tan, Z. Peng, Y. Cao, and G. Hu, *J. Alloys Compd.*, **614**, 264 (2014).
92. Y. Cho, S. Lee, Y. Lee, T. Hong, and J. Cho, *Adv. Energy Mater.*, **1**, 821 (2011).